**Wave Propagation in Finite Element and Mass-Spring-Dashpot Lattice Models**
by
**Marianne S. Holt-Phoenix**
B.S., Mathematics
United States Naval Academy, 2000

SUBMITTED TO THE DEPARTMENT OF MECHANICAL ENGINEERING IN PARTIAL
FULFILLMENT OF THE REQUIREMENTS FOR THE DEGREES OF

NAVAL ENGINEER
AND
MASTER OF SCIENCE IN MECHANICAL ENGINEERING
AT THE
MASSACHUSETTS INSTITUTE OF TECHNOLOGY

JUNE 2006
© 2006 Marianne S. Holt-Phoenix. All rights reserved.

The author hereby grants to MIT and the U.S. Government permission to reproduce and to
distribute publicly paper and electronic copies of this thesis document in whole or part.

Signature of Author_____
Department of Mechanical Engineering
May 8, 2006

Certified by_____
James H. Williams, Jr., School of Engineering Professor of Teaching Excellence
Department of Mechanical Engineering
Thesis Supervisor

Certified by_____
David V. Burke, Senior Lecturer
Department of Mechanical Engineering
Thesis Reader

Accepted by_____
Michael Triantafyllou, Professor of Mechanical and Ocean Engineering
Director, Center for Ocean Engineering
Department of Mechanical Engineering

Accepted by_____
Lallit Anand, Professor of Mechanical Engineering
Chair, Department Committee on Graduate Students
Department of Mechanical Engineering

1

| 1. REPORT DATE<br>**01 JUN 2006** | 2. REPORT TYPE<br>**N/A** | 3. DATES COVERED<br>**-** |
|---|---|---|

| 4. TITLE AND SUBTITLE<br>**Wave Propagation in Finite Element and Mass-Spring-Dashpot Lattice Models** | 5a. CONTRACT NUMBER<br>**N62271-97-G-0026** |
|---|---|
| | 5b. GRANT NUMBER |
| | 5c. PROGRAM ELEMENT NUMBER |

| 6. AUTHOR(S) | 5d. PROJECT NUMBER |
|---|---|
| | 5e. TASK NUMBER |
| | 5f. WORK UNIT NUMBER |

| 7. PERFORMING ORGANIZATION NAME(S) AND ADDRESS(ES)<br>**Massachusetts Institute of Technology** | 8. PERFORMING ORGANIZATION REPORT NUMBER |
|---|---|

| 9. SPONSORING/MONITORING AGENCY NAME(S) AND ADDRESS(ES) | 10. SPONSOR/MONITOR'S ACRONYM(S) |
|---|---|
| | 11. SPONSOR/MONITOR'S REPORT NUMBER(S) |

| 12. DISTRIBUTION/AVAILABILITY STATEMENT<br>**Approved for public release, distribution unlimited** |
|---|

| 13. SUPPLEMENTARY NOTES<br>**The original document contains color images.** |
|---|

| 14. ABSTRACT |
|---|

| 15. SUBJECT TERMS |
|---|

| 16. SECURITY CLASSIFICATION OF: | | | 17. LIMITATION OF ABSTRACT | 18. NUMBER OF PAGES | 19a. NAME OF RESPONSIBLE PERSON |
|---|---|---|---|---|---|
| a. REPORT<br>**unclassified** | b. ABSTRACT<br>**unclassified** | c. THIS PAGE<br>**unclassified** | **UU** | **64** | |

**Wave Propagation in Finite Element and Mass-Spring-Dashpot Lattice Models**
by
**Marianne S. Holt-Phoenix**

Submitted to the Department of Mechanical Engineering in Partial Fulfillment of the Requirements for the Degrees of Naval Engineer and Master of Science in Mechanical Engineering.

## Abstract

Numerical efficiency comparisons of a four-node finite element model (FEM), a mass-spring lattice model (MSLM), and a mass-spring-dashpot lattice model (MSDLM) are investigated. Specifically, the error in the ultrasonic phase speed with variations in Poisson's ratio and angle of incidence is evaluated in each model of an isotropic elastic solid. With regard to phase speed, materials with constant N grid spaces per P-wavelength having Poisson's ratios between 0.0 and 0.25 are modeled more accurately with the MSLM. Materials with Poisson's ratios between 0.35 and 0.5 and N grid spaces per P-wavelength are more accurately modeled with the FEM. Materials whose Poisson's ratio is between 0.25 and 0.35 are modeled equally accurately. With regard to phase speed, viscoelastic materials modeled with FEM and MSDLM show good agreement with known analytical solutions. The computational expense of all three models is also examined. The number of floating point operations (FLOPS) needed to achieve a specified phase speed accuracy is calculated for each different model. While the FEM and MSLM have nearly the same computation cost, the MSDLM is 5 times more costly than either the FEM or MSLM.

Thesis Supervisor: James H. Williams, Jr.
Title: School of Engineering Professor of Teaching Excellence

Thesis Reader: David V. Burke
Title: Senior Lecturer, Department of Mechanical Engineering

Page intentionally left blank

## Acknowledgements

To my advisor Prof. J. H. Williams, Jr., whose guidance and supervision kept me focused and on track over the course of the past year, thank you. You have shown me what a truly great professor is and I will always be grateful for the opportunity I had to work with you.

To Dr. Anton Thomas, who helped me to develop the concepts for this thesis, thank you. Your assistance and encouragement throughout this entire thesis were invaluable.

To my parents Shinko and Wayne for their love and understanding, thank you.

To all my friends and family, who constant encouragement and support kept me motivated, thank you.

To the U.S. Navy for their financial support, thank you.

And finally, I would like to thank my husband Dionisio for your love, patience and absolute confidence in me. I could not have finished my thesis without you.

Page intentionally left blank

# Table of Contents

Page intentionally left blank

# List of Figures

## Introduction

Nondestructive evaluation (NDE) techniques have been used for decades to characterize materials and inspect products. For example, the U.S. Navy has developed a variety of NDE techniques and systems for identifying defects in ship structures. These techniques and systems are vital for finding defects before they impact the safety and mission readiness of a ship [1]. Most NDE systems contain an energy source used to probe an object, a receiver or detector that measures how the energy has been changed by the object, and components and analyses to record, process, and interpret the measurement data [2]. Many of these systems use ultrasonic wave energy. Some advantages of ultrasonic testing (UT) are that small surface and subsurface discontinuities can be detected. Ideally, the approximate size and orientation of the flaw can also be determined [3]. Prediction and simulation of ultrasonic wave propagation provide valuable analytical techniques in the interpretation of UT data.

Two approaches to numerical simulation of wave propagation are with a finite element model (FEM) and a mass-spring-dashpot lattice model (MSDLM). Finite element procedures are now a critical part of engineering analysis and design [4]. The versatility and ease of use of commercially available finite element programs have contributed to their popularity. In recent years, new research in mass-spring lattice models has taken place. Yim [5] discusses the advantages of a mass-spring lattice model and the U.S. Navy has already begun research in numerical simulation of thick, layered composites with mass-spring-dashpot lattice models [6]. In this thesis, FEM and MSDLM are compared with regard to phase speed accuracy and computational cost.

## Problem Statement

Choosing an appropriate analysis method can be difficult without knowing which model will most accurately represent a particular material or phenomenon.

Numerical anisotropy exists in each model and may affect computational results, especially with regard to propagation direction [7]. It is well known that one method of reducing error is by reducing mesh size. This does have the added effect of increasing computational cost. This thesis proposes that by choosing carefully the model used, error and computational cost may be reduced.

## Introduction to Numerical Models

The mass-spring-dashpot lattice model (MSDLM) in Fig.1 [8] is a modified version of the mass-spring lattice model (MSLM) of Yim and Sohn [9] and Yim and Choi [10]. The MSDLM is a heuristic, physical model where the inertia and viscoelasticity of a solid are modeled as particles interconnected with springs and dashpots.

The spring constants and dashpot coefficients are derived from the exact partial differential equations governing a two-dimensional standard linear solid [8]. The particle velocities and displacements, as well as volumetric forces through each element are numerically integrated with a fourth-order Runge-Kutta algorithm [11]. The MSDLM has been used to study wave propagation phenomena in materials having attenuation and has been shown to agree with analytical solutions in both steady-state and transient analyses [8].

(a)
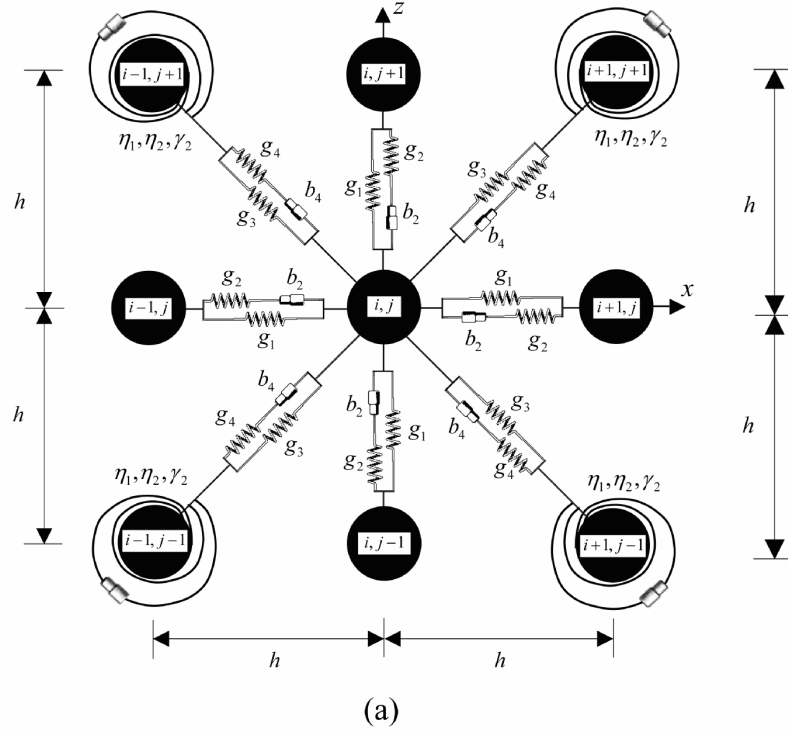
**Figure 1.** Schematic of an MSDLM at an interior plane-strain particle located at position $(i, j)$ [8].

To ensure stability and convergence of the Runge-Kutta algorithm in the MSDLM, the Courant number $C$ must satisfy

$$C \equiv \frac{c_{\max,P} \Delta t}{h} \leq 1.30 \tag{1}$$

where $c_{max,P}$ is the maximum $P$ phase speed, $h$ is the grid space, and $\Delta t$ is the numerical time step [8]. Phase speed is the speed at which the crest of a single-frequency wave travels.

The finite element method is an approach for solving partial differential equations (PDEs) and integral equations [12]. Finite element modeling of a solution involves the mesh discretization of a continuous domain into a set of discrete sub-domains and a finite number of points called nodes. In Fig. 2, elements comprising the entire domain are connected at common nodes and collectively approximate the shape of the initial domain. The elements

13

are then approximated by a discrete set of piecewise continuous functions (polynomials) defined using the nodal values of the continuous solution. The solution to the piecewise continuous functions approximates the solution to the initial PDE. Finite difference methods are different from finite element methods in that the differential operators are approximated rather than represented by piecewise polynomials.



**Figure 2**. Schematic of a four-node FEM at an interior plane-strain node located at position $(i, j)$.

In structural mechanics, finite element methods are often based on an energy principle such as the principle of virtual work. Polynomial shape functions are used to relate the displacement at any particular point to the displacements at the FEM nodes. A model of a material such as a standard linear solid can be generated using the displacements at the nodes,

material properties, and constitutive relationships. FEM have been used to study wave

propagation and attenuation and have been shown to agree with analytical solutions.

To ensure accuracy and stability in a wave propagation finite element model, certain

criteria must be met. The length, $L_e$, of a finite element must be

$$L_e = c_{max} \Delta t \qquad (2)$$

where $c$ is the maximum wave speed and $\Delta t$ is the corresponding timestep. For this analysis, an

explicit integration method is used which means the Courant-Friedrichs-Lewy (CFL) condition

must be met in order to obtain accurate results. Simply stated, the maximum allowable Courant

number $C$ that an explicit time-integrator may use is 1.

$$C \equiv \frac{c_{max} \Delta t}{L_e} \qquad (3)$$

where $L_e$ corresponds to the length of the finite element $h$. While it is well known that $C$ greater

than 1 causes a model to become unstable, a finite element model also becomes inaccurate as $C$

decreases to values less than 1 [12].

Fig.3 is a mass-spring-lattice model (MSLM). It is similar to the MSDLM in arrangement

of nodes but differs from the MSDLM in that it lacks dashpots. It is useful in modeling wave

propagation phenomena in elastic materials and has been shown to agree with analytical

solutions in both steady-state and transient analyses [5,9,10].

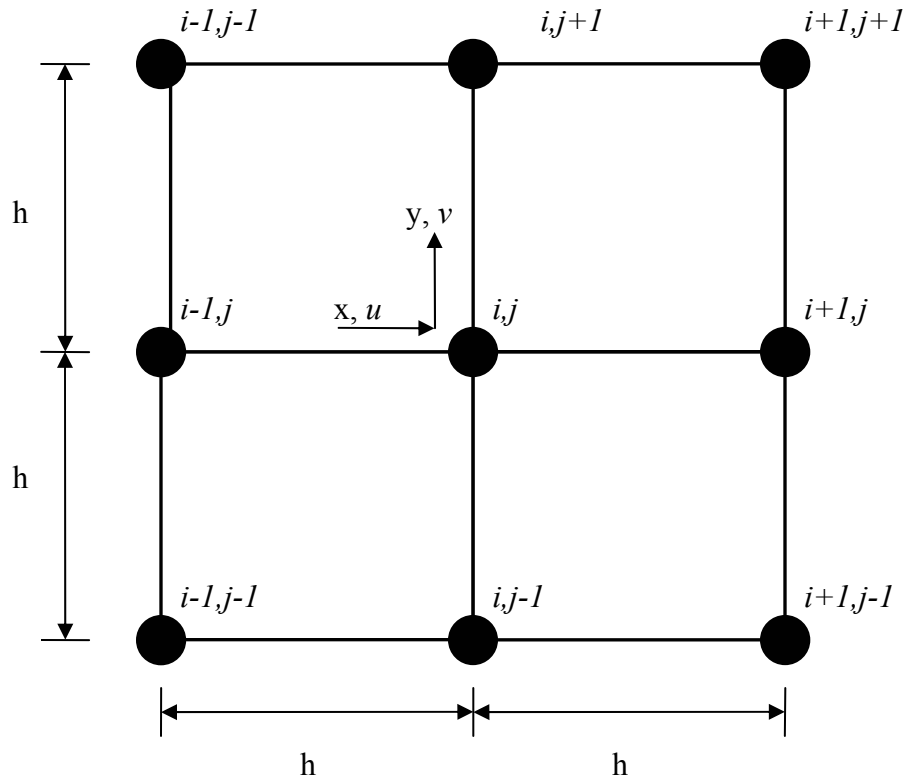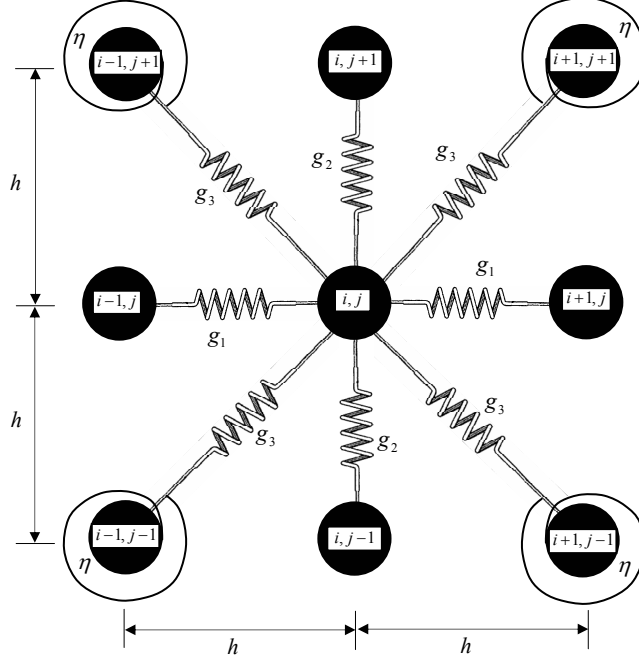**Figure 3**. Schematic of MSLM at an interior plane-strain particle located at position $(i, j)$ [8].

## Investigation into Accuracy of an Interior Point

In this example, the material is elastic and does not attenuate, so the mass-spring-lattice

model (MSLM) is used. The phase speed accuracy can be investigated using the MSLM and a

four-node FEM with an arbitrarily oriented plane wave propagating through an unbounded

elastic media.

The equations of motion in a plane strain isotropic medium having mass proportional

damping expressed in Cartesian coordinates, are

$$\rho\frac{\partial^2 u}{\partial t^2} = (\lambda + 2\mu)\frac{\partial^2 u}{\partial x^2} + (\lambda + \mu)\frac{\partial^2 v}{\partial x \partial y} + \mu\frac{\partial^2 u}{\partial y^2} - \frac{\rho}{\tau}\frac{\partial u}{\partial t} \tag{4}$$

$$\rho\frac{\partial^2 v}{\partial t^2} = (\lambda + 2\mu)\frac{\partial^2 v}{\partial y^2} + (\lambda + \mu)\frac{\partial^2 u}{\partial x \partial y} + \mu\frac{\partial^2 v}{\partial x^2} - \frac{\rho}{\tau}\frac{\partial v}{\partial t} \tag{5}$$

where $u$ is the displacement in the $x$-direction, $v$ is the displacement in the $y$-direction, $\rho$ is the

density, $\tau$ is a time constant, and $\lambda$ and $\mu$ are Lamé elastic constants.

The four node finite element model discretization of eqn. (4) and eqn. (5) give the following equations written in component form at a particle position $(i,j)$ at time $t$.[Appendix A]

$$^{t+\Delta t}u_{i,j}\left(\rho\frac{1}{(\Delta t)^2}+\frac{\rho}{\tau}\frac{1}{2\Delta t}\right)=-^{t-\Delta t}u_{i,j}\left(\rho\frac{1}{(\Delta t)^2}-\frac{\rho}{\tau}\frac{1}{2\Delta t}\right)+2\,^tu_{i,j}\left(\rho\frac{1}{(\Delta t)^2}\right)$$

$$+\frac{\frac{2}{3}\lambda+\mu}{h^2}\left(^tu_{i+1,j}+^tu_{i-1,j}-2\,^tu_{i,j}\right)-\frac{\frac{1}{3}\lambda}{h^2}\left(^tu_{i,j+1}+^tu_{i,j-1}-2\,^tu_{i,j}\right)$$

$$+\frac{\frac{1}{6}\lambda+\frac{1}{2}\mu}{h^2}\left(^tu_{i+1,j+1}+^tu_{i-1,j+1}+^tu_{i-1,j-1}+^tu_{i+1,j-1}-4\,^tu_{i,j}\right)$$

$$+\frac{\frac{1}{4}\lambda+\frac{1}{4}\mu}{h^2}\left(^tv_{i+1,j+1}-^tv_{i-1,j+1}+^tv_{i-1,j-1}-^tv_{i+1,j-1}\right)$$

$$(6)$$

$$^{t+\Delta t}v_{i,j}\left(\rho\frac{1}{(\Delta t)^2}+\frac{\rho}{\tau}\frac{1}{2\Delta t}\right)=-^{t-\Delta t}v_{i,j}\left(\rho\frac{1}{(\Delta t)^2}-\frac{\rho}{\tau}\frac{1}{2\Delta t}\right)+2\,^tv_{i,j}\left(\rho\frac{1}{(\Delta t)^2}\right)$$

$$\frac{\frac{2}{3}\lambda+\mu}{h^2}\left(^tv_{i,j+1}+^tv_{i,j-1}-^t2v_{i,j}\right)-\frac{\frac{1}{3}\lambda}{h^2}\left(^tv_{i+1,j}+^tv_{i-1,j}-2\,^tv_{i,j}\right)$$

$$+\frac{\frac{1}{6}\lambda+\frac{1}{2}\mu}{h^2}\left(^tv_{i+1,j+1}+^tv_{i+1,j-1}+^tv_{i-1,j-1}+^tv_{i-1,j+1}-4\,^tv_{i,j}\right)$$

$$+\frac{\frac{1}{4}\lambda+\frac{1}{4}\mu}{h^2}\left(^tu_{i+1,j+1}-^tu_{i+1,j-1}+^tu_{i-1,j-1}-^tu_{i-1,j+1}\right)$$

$$(7)$$

where $\Delta t$ is the numerical time step and $h$ is the grid spacing. (A similar analysis for the MSLM can be found in reference [8].) For stability, the Courant number $C$ must satisfy

$$C\equiv\frac{c_P\Delta t}{h}\le 1 \tag{8}$$

where $c_P$ is the longitudinal wave speed given by

$$c_P=\sqrt{\frac{\lambda+2\mu}{\rho}} \tag{9}$$

The shear wave speed $c_S$ is given by

$$c_S=\sqrt{\frac{\mu}{\rho}} \tag{10}$$

## *Analysis of accuracy*

Taking the two dimensional discrete Fourier transform of eqn (3) and (4) and forming the

amplification equation yields [8]

$$^{t+\Delta t}\mathbf{u} = \mathbf{G}\,^{t}\mathbf{u} \tag{11}$$

where

$$^{t}\mathbf{u} = \begin{bmatrix} ^{t}U & ^{t}V & ^{t-\Delta t}U & ^{t-\Delta t}V \end{bmatrix} \tag{12}$$

$$^{t+\Delta t}\mathbf{u} = \begin{bmatrix} ^{t+\Delta t}U & ^{t+\Delta t}V & ^{t}U & ^{t}V \end{bmatrix} \tag{13}$$

$$\mathbf{G} = \begin{bmatrix} a & b & c & 0 \\ d & e & 0 & f \\ 1 & 0 & 0 & 0 \\ 0 & 1 & 0 & 0 \end{bmatrix} \tag{14}$$

and where

$$a = \frac{\left[ \begin{array}{l} \left[ \left( \left( \dfrac{2(2\lambda+3\mu)}{3h^{2}} \right)(\cos(k_{x}h)-1) \right) - \left( \left( \dfrac{2\lambda}{3h^{2}} \right)(\cos(k_{y}h)-1) \right) \right] \\ + \left( \dfrac{4(\lambda+3\mu)}{6h^{2}} \right)(\cos(k_{y}h)(\cos(k_{x}h))-1) + \left( \dfrac{2\rho}{(\Delta t)^{2}} \right) \end{array} \right]}{\dfrac{\rho}{(\Delta t)^{2}} + \dfrac{\rho}{2\tau\Delta t}} \tag{15}$$

$$b = \frac{-\dfrac{\lambda+\mu}{h^{2}}\left( \sin(k_{x}h)\sin(k_{y}h) \right)}{\dfrac{\rho}{(\Delta t)^{2}} + \dfrac{\rho}{2\tau\Delta t}} \tag{16}$$

$$c = \frac{-\left( \dfrac{\rho}{(\Delta t)^{2}} - \dfrac{\rho}{2\tau\Delta t} \right)}{\dfrac{\rho}{(\Delta t)^{2}} + \dfrac{\rho}{2\tau\Delta t}} \tag{17}$$

$$d = \frac{-\dfrac{\lambda + \mu}{h^2}\left(\sin(k_x h)\sin(k_y h)\right)}{\dfrac{\rho}{(\Delta t)^2} + \dfrac{\rho}{2\tau\Delta t}} \tag{18}$$

$$e = \frac{\left[\begin{array}{l}\left(\left(\dfrac{2(2\lambda + 3\mu)}{3h^2}\right)\left(\cos(k_y h) - 1\right)\right) - \left(\left(\dfrac{2\lambda}{3h^2}\right)\left(\cos(k_x h) - 1\right)\right) \\[2mm] + \left(\dfrac{4(\lambda + 3\mu)}{6h^2}\right)\left(\cos(k_y h)\left(\cos(k_x h)\right) - 1\right) + \left(\dfrac{2\rho}{(\Delta t)^2}\right)\end{array}\right]}{\dfrac{\rho}{(\Delta t)^2} + \dfrac{\rho}{2\tau\Delta t}} \tag{19}$$

$$f = \frac{-\left(\dfrac{\rho}{(\Delta t)^2} - \dfrac{\rho}{2\tau\Delta t}\right)}{\dfrac{\rho}{(\Delta t)^2} + \dfrac{\rho}{2\tau\Delta t}} \tag{20}$$

In eqns. (12) through (17)

$$k_x = k\cos\theta \tag{21}$$

$$k_y = k\sin\theta \tag{22}$$

The four eigenvectors of the amplification matrix $\mathbf{G}$ are $\xi_{+P}$, $\xi_{+S}$, $\xi_{-P}$, and $\xi_{-S}$, where the subscripts + or − refer to the positive and negative phases.

The positive phase change in one time step is found from the exact dispersion relation as

$$\omega_{exact}\Delta t = kc_P\Delta t \tag{23}$$

$$\omega_{exact}\Delta t = kc_S\Delta \tag{24}$$

and the positive phase change from the numerical approximation is [13]

$$\omega_{numerical}\Delta t = \text{Im}\{\ln(\xi_{+P})\} \tag{25}$$

$$\omega_{numerical}\Delta t = \text{Im}\{\ln(\xi_{+S})\} \tag{26}$$

where $\xi_P$, and $\xi_S$ are the eigenvectors that correspond to the pressure or $P$- and shear or $S$-waves.

The numerical phase change can be written in non-dimensional form as

$$\omega_{numerical}\Delta t = fcn\{C, v, kh, \theta, \omega\tau\} \tag{27}$$

where $v$ is the Poisson's ratio, $\omega\tau$ is a non-dimensional frequency, $k$ is the wavenumber, and $h$ is the grid spacing. (A similar analysis for the MSLM can be found in reference [8].)

Percent phase error in the numerical phase change relative to the exact phase change is defined

$$\frac{\omega_{numerical}\Delta t - \omega_{exact}\Delta t}{\omega_{exact}\Delta t} \times 100\% \tag{28}$$

Multiplying eqn. (25) by

$$\frac{1/k}{1/k} \tag{29}$$

yields

$$\varepsilon_c = \frac{c_{numerical} - c_{exact}}{c_{exact}} \times 100\% \tag{30}$$

which is simply the percent error in wave speed.

Consider the exact and numerical dispersion relation for an elastic material with $v$=0.30 and a plane wave propagating along the $x$-axis ($\theta$=0) as shown in Fig. 4. For this example and for the remainder of this paper, $C$=1 will be used. As seen in the figure, the phase error of $P$-waves of both FEM and MSLM rapidly decrease despite the small number of grid spaces per wavelength. This phenomena is due to the fact that the FEM and the MSLM solutions are equal to the exact solution for this Poisson's ratio $v$=0.30 and angle of orientation $\theta$=0°. The $S$-wave propagation of the FEM and MSLM differ as the normalized wavelength increases. It is interesting to note that the $S$-wave phase speed error is the same for both models at Poisson's ratio $v$=0.3 and angle of orientation $\theta$=0°.

Fig. 5 shows the case where Poisson's ratio $v$=0.3 and angle of orientation $\theta$=45°.

The only difference between Fig. 4 and Fig. 5 is the angle of orientation. The FEM $P$-wave error is now significantly different due to the change in $\theta$. The $P$-wave solution changed from the exact solution to a solution that has an error inversely proportional to the number of grid spaces. In the FEM, the $P$- and $S$- wave phase speed errors are nearly equal but the errors in the $P$- and $S$-waves for the MSLM are different by a factor of two. The unusual behavior of the MSLM $S$-wave is disregarded due to the small number of grid spaces per wavelength. At two grid spaces per wavelength, both models are extremely inaccurate.

While it is well known that the phase errors in most numerical models vary as $\theta$ varies, it is interesting to note that the phase error in each model varies as $v$ varies as well. In Fig. 6, $\theta = 45°$ and $v = 0.2$. The phase error of the MSLM is clearly less than the phase error of the FEM. The difference in error between the FEM and the MSLM equates to roughly one less grid spacing per wavelength.

In Fig. 7, $\theta = 45°$ and $v = 0.4$. The phase speed error for the $P$-wave speed in the FEM is slightly larger than the phase speed error in the MSLM. However, the $S$-wave speed error is nearly one order of magnitude smaller in the FEM than in the MSLM.

(a)



(b)
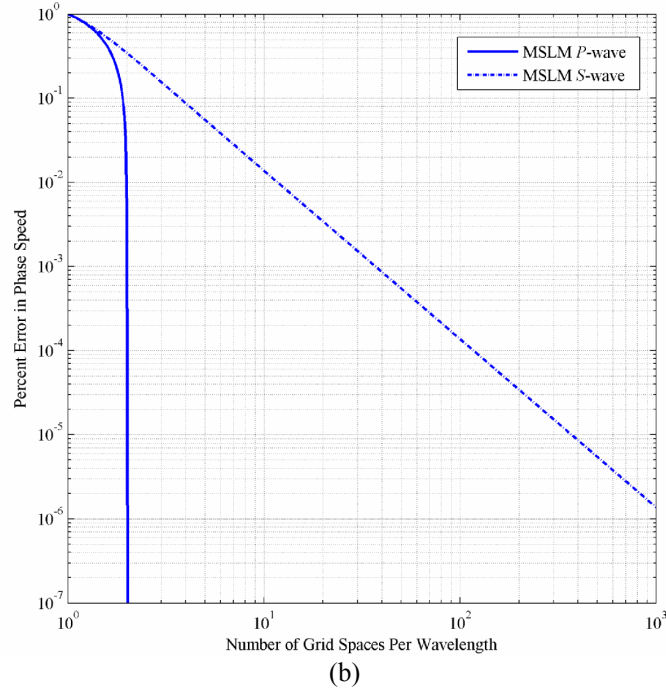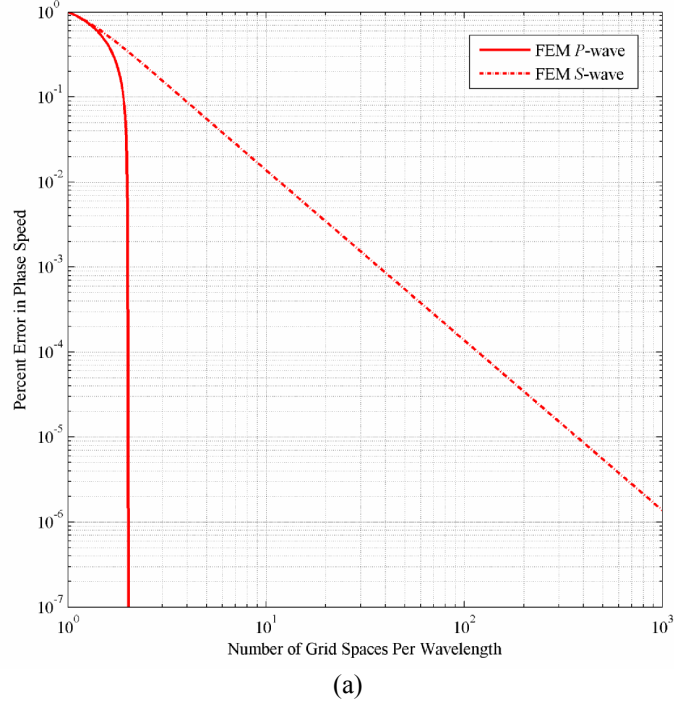
**Figure 4**. Percent error in phase speed as a function of grid spaces per wavelength, where Poisson's ratio $v$ =0.3 and angle of orientation $\theta$ =0° for (a) FEM and (b) MSLM.
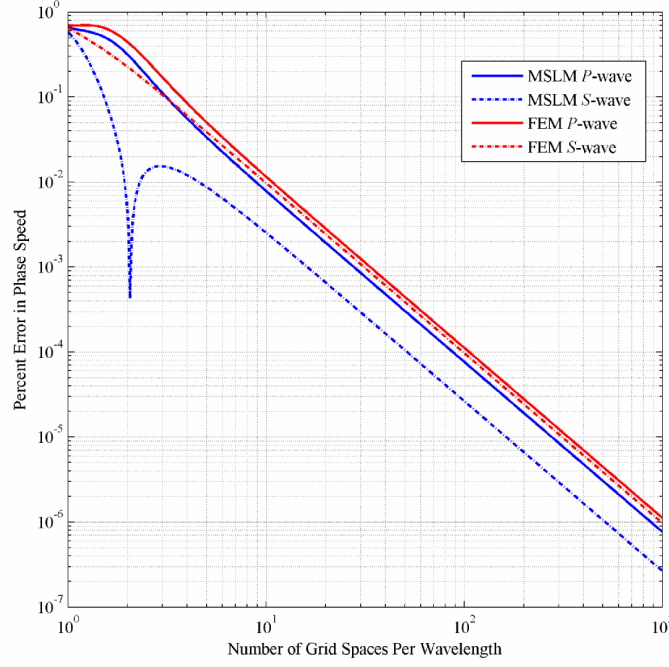
**Figure 5**. Percent error in phase speed as a function of grid spaces per wavelength, where the Poisson's ratio $v$ =0.3 and angle of orientation $\theta$ =45°.
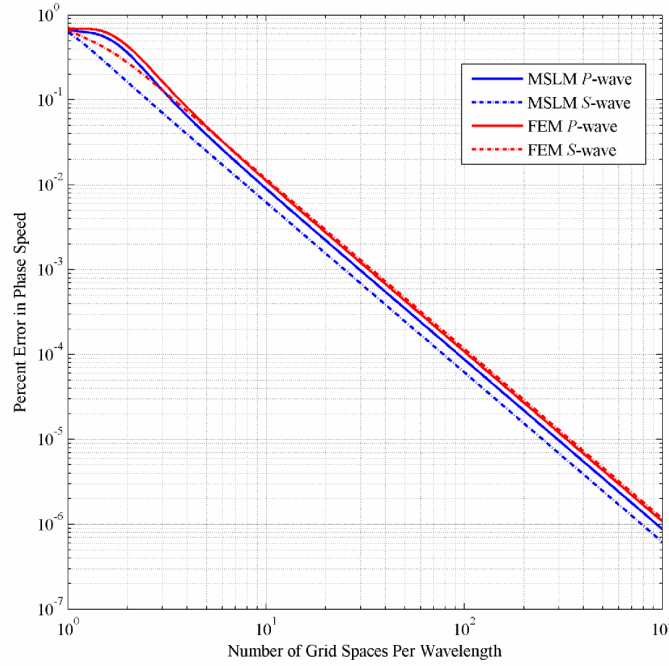


**Figure 6**. Percent error in phase speed as a function of grid spaces per wavelength, where Poisson's ratio $v$ =0.2 and angle of orientation $\theta$ =45°.
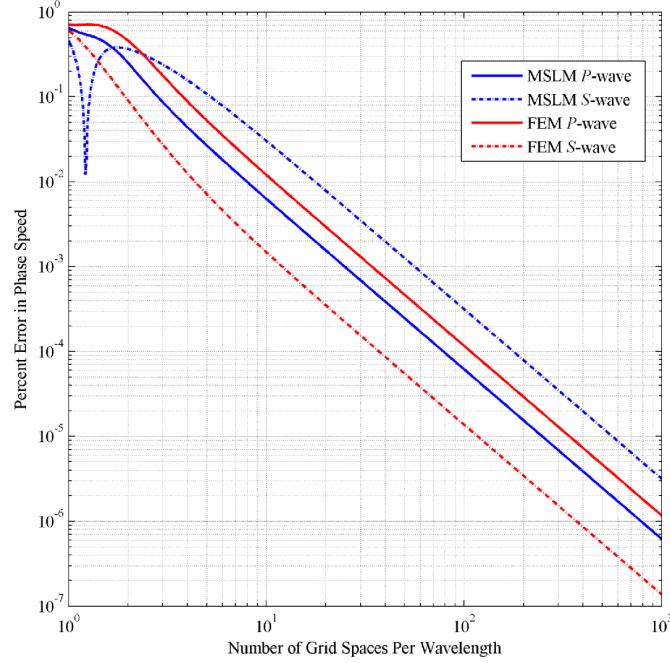
**Figure 7**. Percent error in phase speed as a function of grid spaces per wavelength, where Poisson's ratio $v = 0.4$ and angle of orientation $\theta = 45°$.

Typically, in engineering applications an acceptable error is known and grid spaces per wavelength N are determined and given by

$$N_P = \frac{2\pi}{k_p h} \tag{31}$$

$$N_S = \frac{2\pi}{k_S h} \tag{32}$$

where $N_P$ and $N_S$ are the number of grid spaces per $P$ and $S$ wavelengths respectively, $k_P$ and $k_S$ are the respective wavenumbers, and $h$ is the grid space.

Figure 9 is the number of grid spaces required by the MSLM to achieve 1% error or less in phase speed as functions of Poisson's ratio and angle of incidence. Fig.10 is the same plot for the FEM. Note that for both the FEM and MSLM, $N_P$ and $N_S$ are symmetric about $\theta = 45°$, which follows from the symmetry of the models for interior particles as shown in Fig. 2 and Fig. 3. In

both models, the phase error of $P$-waves decays to zero as $\theta \rightarrow 0°$. Holding $\theta = 0°$ or $90°$, $N_S$ is a monotonically increasing function for both FEM and MSLM

There are differences in the models. In the MSLM, $N_P$ decreases as $v$ increases while holding $\theta = 45°$. In the FEM, holding $\theta = 45°$ and increasing $v$ increases $N_P$ slightly. Holding $\theta = 45°$, $N_S$ for MSLM has a minimum at $v = 0.3$ before increasing dramatically. The FEM has a minimum $N_S$ at $v = 0.43$ before increasing. The errors in $S$-wave speed for the case when $\theta = 45°$ and $v$ varies from 0.0 to 0.5 is shown in Fig. 8.

Page intentionally left blank
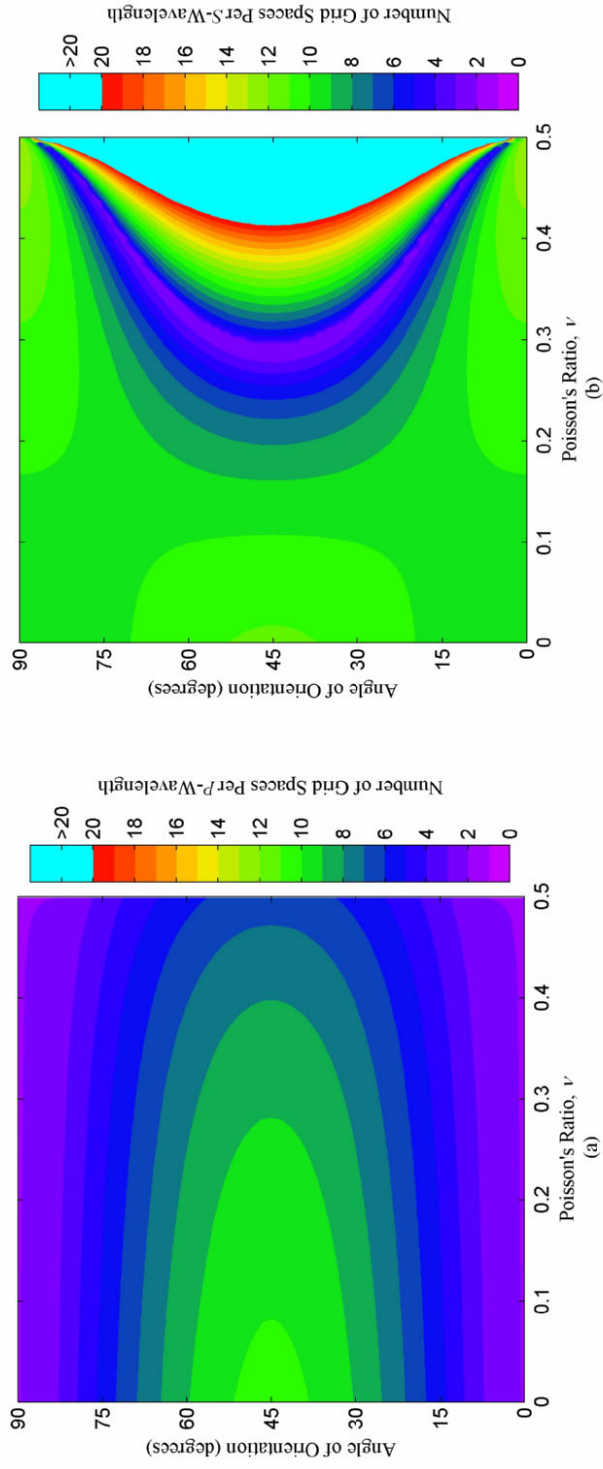
**Figure 8**. Number of grid spaces per wavelength required to achieve 1% or less phase speed error in MSLM as a function of Poisson's ratio $v$, and a plane wave angle of incidence $\theta$ with respect to the horizontal axis for (a) $P$ waves and (b) $S$ waves.

27

Page intentionally left blank
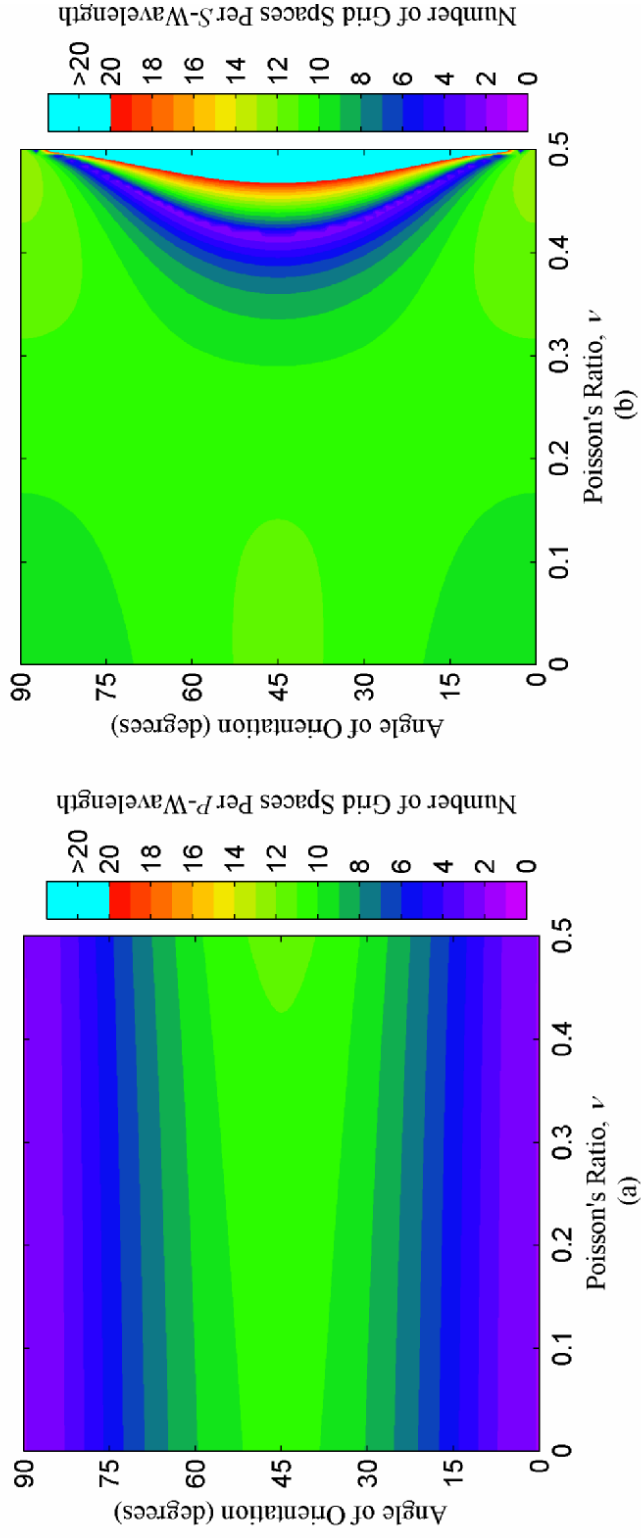
**Figure 9**. Number of grid spaces per wavelength required to achieve 1% error or less phase speed error in FEM as a function of Poisson's ratio $v$ and plane wave angle of incidence $\theta$ with respect to horizontal axis for (a) $P$ waves and (b) $S$ waves.

29
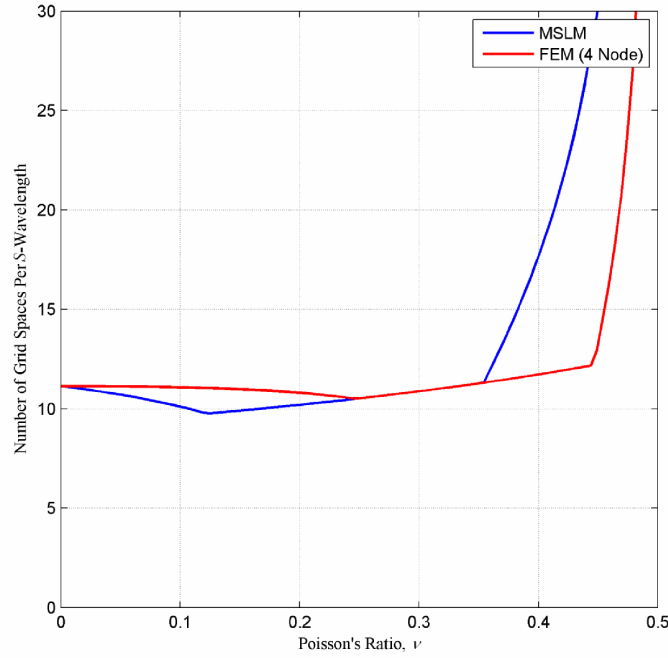
**Figure 10**. Number of grid spaces required for 1% phase speed error for S-waves as *v* varies from 0.0 to 0.5 angle of incidence *θ* =45°.

## Investigation into Accuracy of a Point at a Traction Free Surface

Wave propagation problems involving a surface excitation and a surface response in an elastic half-space have become known as Lamb's problems due to the efforts of Horace Lamb in 1904. Lamb's work is based on Rayleigh's discovery of surface waves in 1887. Lamb discovered Rayleigh waves are a direct function of the source kinematics and that *P*- and *S*-waves are a function of the time derivative of the source function [14]. An analytical solution exists for these types of problems. (Refer to [8] or [15] for a detailed discussion of the analytical solution.)

Previously in this paper, FEM and MSLM were compared to each other for phase speed accuracy at an interior point. FEM and MSLM displacement accuracy will be compared to an analytical solution for a point on a traction-free boundary.

Two dimensional schematics of the FEM and the MSLM discretization of a plane strain

elastic solid at a traction free boundary are shown in Fig. 11 and Fig. 12. The corresponding

equations of motion in indicial notation for the FEM are

$$
\begin{aligned}
\rho \frac{1}{\Delta t^2}\left({}^{t-\Delta t}u_{i,j} - 2\,{}^{t}u_{i,j} + {}^{t+\Delta t}u_{i,j}\right) + \frac{\rho}{\tau}\frac{1}{2\Delta t}\left(-{}^{t-\Delta t}u_{i,j} + {}^{t+\Delta t}u_{i,j}\right) &= \frac{\frac{2}{3}\lambda+\mu}{h^2}\left({}^{t}u_{i+1,j} + {}^{t}u_{i-1,j} - 2\,{}^{t}u_{i,j}\right) \\
&\quad -\frac{\frac{2}{3}\lambda}{h^2}\left({}^{t}u_{i,j-1} - {}^{t}u_{i,j}\right) \\
&\quad +\frac{\frac{1}{3}\lambda+\mu}{h^2}\left({}^{t}u_{i-1,j-1} + {}^{t}u_{i+1,j-1} - 2\,{}^{t}u_{i,j}\right) \\
&\quad +\frac{\frac{1}{2}\lambda+\frac{1}{2}\mu}{h^2}\left({}^{t}v_{i-1,j-1} - {}^{t}v_{i+1,j-1}\right) - \frac{\frac{1}{2}\lambda-\frac{1}{2}\mu}{h^2}\left({}^{t}v_{i-1,j} - {}^{t}v_{i+1j}\right)
\end{aligned}
\tag{33}
$$

$$
\begin{aligned}
\rho \frac{1}{\Delta t^2}\left({}^{t-\Delta t}v_{i,j} - 2\,{}^{t}v_{i,j} + {}^{t+\Delta y}v_{i,j}\right) + \frac{\rho}{\tau}\frac{1}{2\Delta t}\left(-{}^{t-\Delta t}v_{i,j} + {}^{t+\Delta t}v_{i,j}\right) &= \frac{\frac{4}{3}\lambda+2\mu}{h^2}\left({}^{t}v_{i,j-1} - {}^{t}v_{i,j}\right) \\
&\quad -\frac{\frac{1}{3}\lambda}{h^2}\left({}^{t}v_{i-1,j} + {}^{t}v_{i+1,j} - 2\,{}^{t}v_{i,j}\right) \\
&\quad +\frac{\frac{1}{3}\lambda+\mu}{h^2}\left({}^{t}v_{i-1,j-1} + {}^{t}v_{i+1,j-1} - 2\,{}^{t}v_{i,j}\right) \\
&\quad +\frac{\frac{1}{2}\lambda+\frac{1}{2}\mu}{h^2}\left({}^{t}u_{i-1,j-1} - {}^{t}u_{i+1,j-1}\right) - \frac{\frac{1}{2}\lambda-\frac{1}{2}\mu}{h^2}\left({}^{t}u_{i+1,j} - {}^{t}u_{i-1,j}\right)
\end{aligned}
\tag{34}
$$

where $\Delta t$ is the numerical time step, and $u_{i,j}$ and $v_{i,j}$ are horizontal and vertical displacements

respectively. (A detailed analysis of the corresponding equations of motion of the MSLM can be

found in reference [8].)
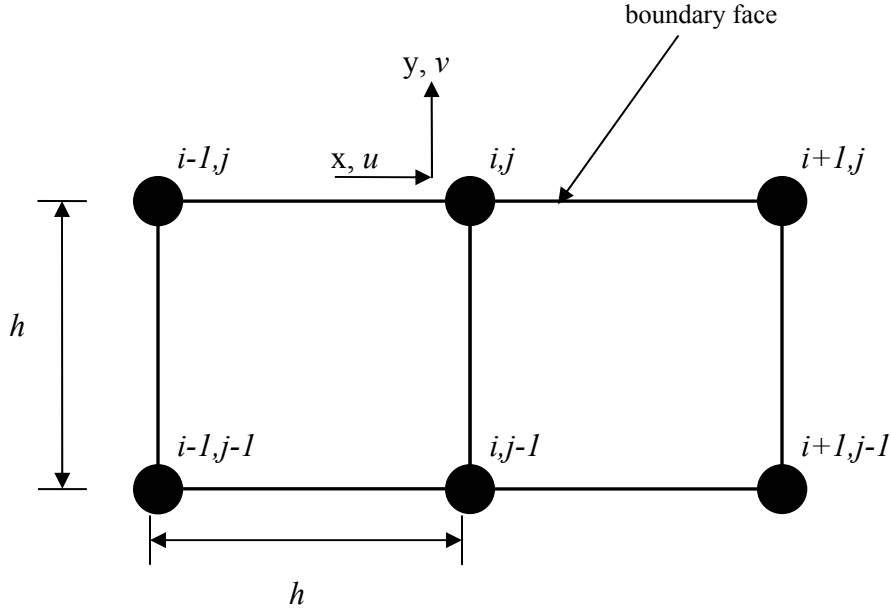
**Figure 11**. Schematic of an FEM at surface plane-strain particle located at position $(i, j)$.
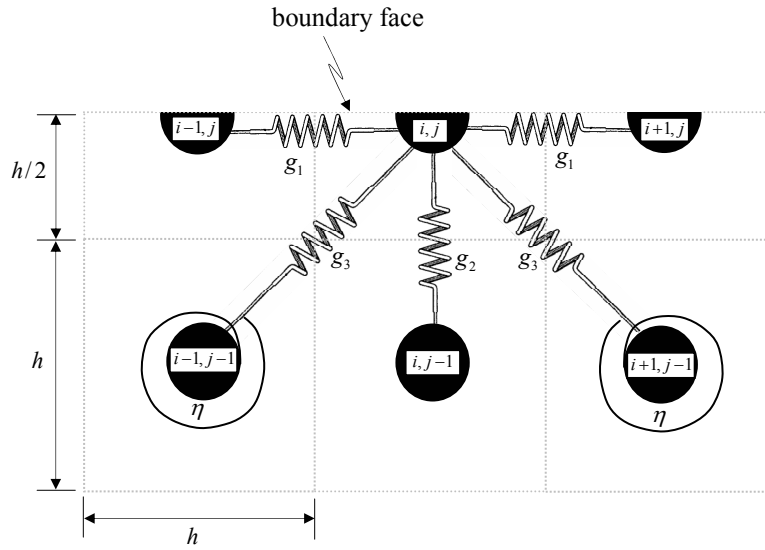


**Figure 12**. Schematic of an MSLM at surface plane-strain particle located at position $(i, j)$ [8].

## *Input Signal Shape*

The surface excitations in the two-dimensional numerical simulations are point loads.

The frequency content of the time-varying point load is dictated by the Gaussian-modulated

cosinusoid depicted in Fig. 13. The numerical function is

$$u(0,t) = u_p \exp\left(-\frac{1}{2}(2\pi f_\sigma t - 3)^2\right)\cos\left(2\pi f_c t - 3 f_c f_\sigma^{-1}\right) \qquad (35)$$
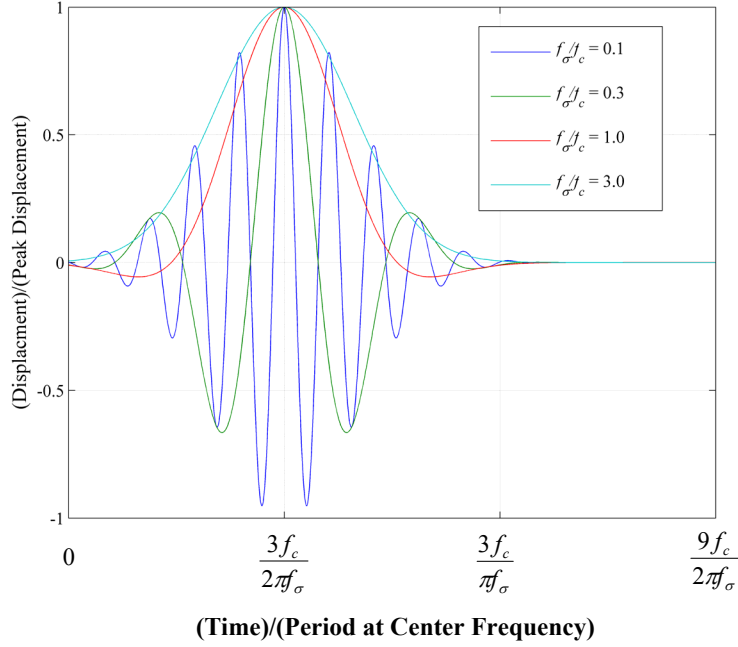


**Figure 13**. Gaussian-modulated cosinusoidal input.

where $u_p$ is the peak displacement, $f_\sigma$ is the standard deviation cyclic frequency, and $f_c$ is the

center cyclic frequency. The maximum effective frequency of the input signal is $f_c + 3 f_\sigma$.

Maximum effective frequency relates to the minimum propagating wavelength. This minimum

wavelength is used in accuracy calculations.

Figure 14 shows the surface displacement of a particle 3.5 *P*-wavelengths from the point

source in the MSLM. Figure 15 shows the surface displacement of a particle 3.5 P-wavelengths

from the point source in the FEM. Twenty grid spaces per minimum wavelength are used in each

model. This grid spacing is selected to ensure less than 1% error in phase speed for an interior

particle for both the FEM and the MSLM.

## *Accuracy*

Both the FEM and MSLM reproduce Lamb's solution for surface displacements of an elastic material due to surface excitation. As shown in Fig. 14 and Fig. 15, the difference between the analytical solution and the numerical solution is small. In the FEM and MSLM, the phase error in both the horizontal and vertical directions is less than 2%. A detailed summary of Lamb's solution appears in Appendix C.
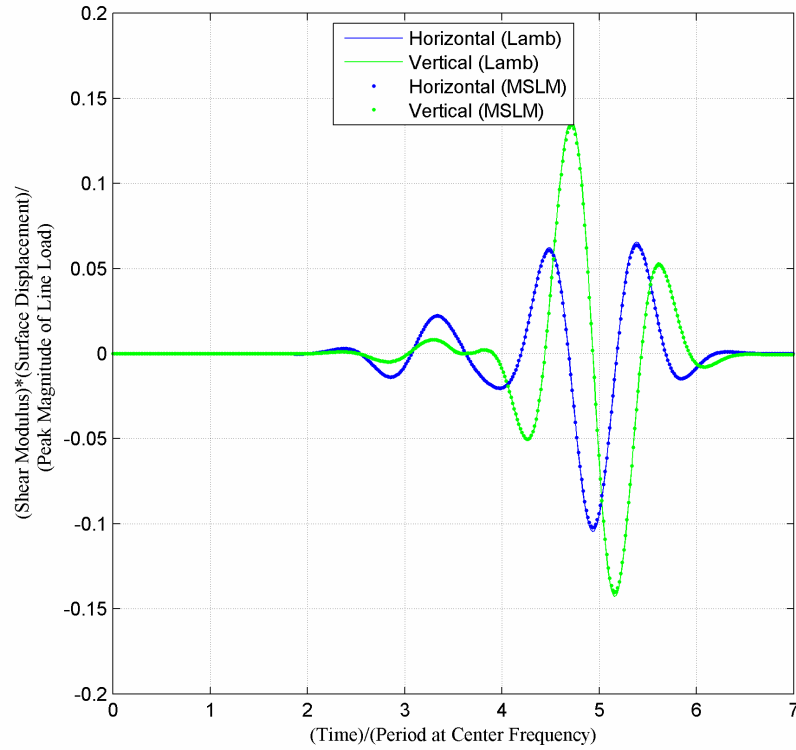


**Figure 14**. Horizontal and vertical displacements of the surface particle located 3.5 P-wavelengths from a point source in the MSLM.
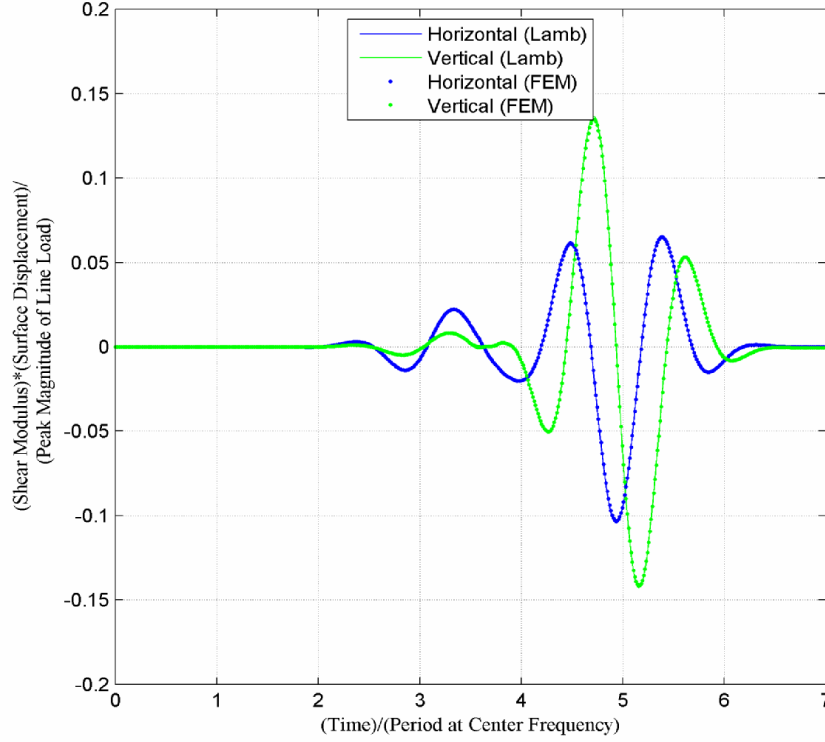
**Figure 15.** Horizontal and vertical displacements of the surface particle located 3.5 P-wavelengths from a point source in the FEM mode.

## Attenuation analysis of FEM and MSDLM

Attenuation is a decrease in the amplitude of a wave due to the material's absorption of energy. Damping is the tendency of a material or system to reduce the amplitude of oscillations. The attenuation of a signal is the result of damping in a material through which a signal is traveling. In lumped parameter models damping is modeled by an element retarding force is proportional to the velocity across it. As shown in Fig. 1, the MSDLM includes dashpots, which act as dampers.

The FEM does not model damping in the above manner. A damping matrix cannot be constructed in the same way as the stiffness matrix in Appendix A. Rayleigh damping is used instead. The equation for Rayleigh damping is [12]

$$\mathbf{C} = \alpha\mathbf{M} + \beta\mathbf{K} \tag{36}$$

35

Where **C** is the damping matrix, **M** is the mass matrix, **K** is the stiffness matrix, and $\alpha$ and $\beta$ are constants determined from two given damping ratios that correspond to two unequal frequencies of vibration. Thus damping in the FEM is not proportional to velocity but is proportional to mass.

In this thesis, one characteristic of damping is penetration depth ($Q$) (Appendix D). This is the depth an input signal travels into a material before the amplitude of the signal is reduced to $e^{-\pi}$ (about 4%) of its original amplitude. Initial results indicate that a damped FEM does agree with numerical solutions determined by the MSDLM. In Fig. 16, the phase speed error of a material with $Q= 25$ is shown.
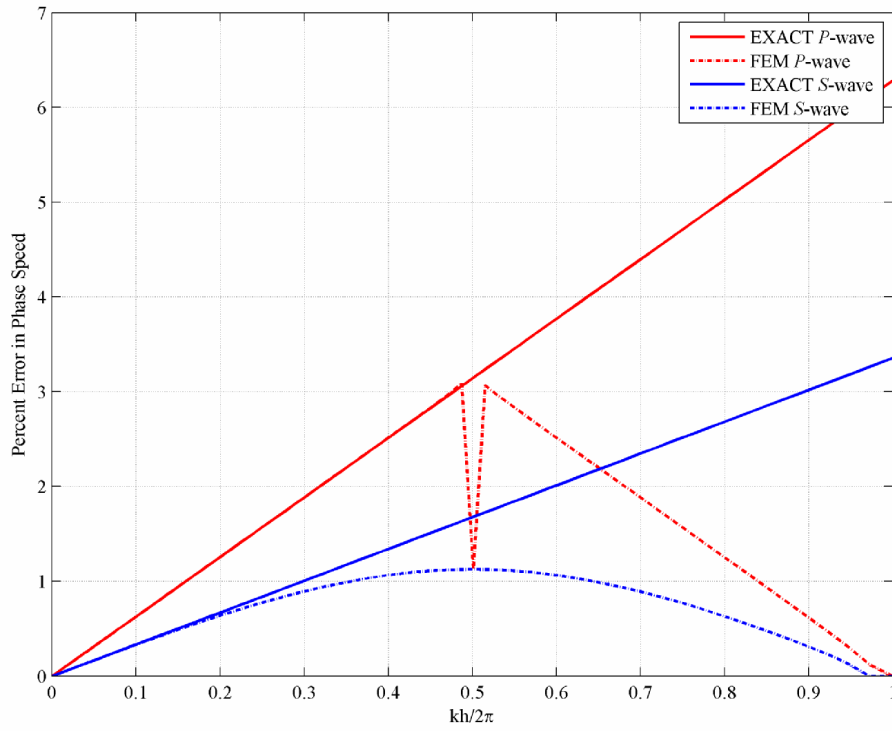


**Figure 16**. Phase speed error of a FEM of a material with $Q$=25 and angle of orientation $\theta$ =45°.

In Fig. 17, the same material is modeled with varying grid spaces per wavelength. This shows good agreement with an analysis of the MSDLM in reference [8].
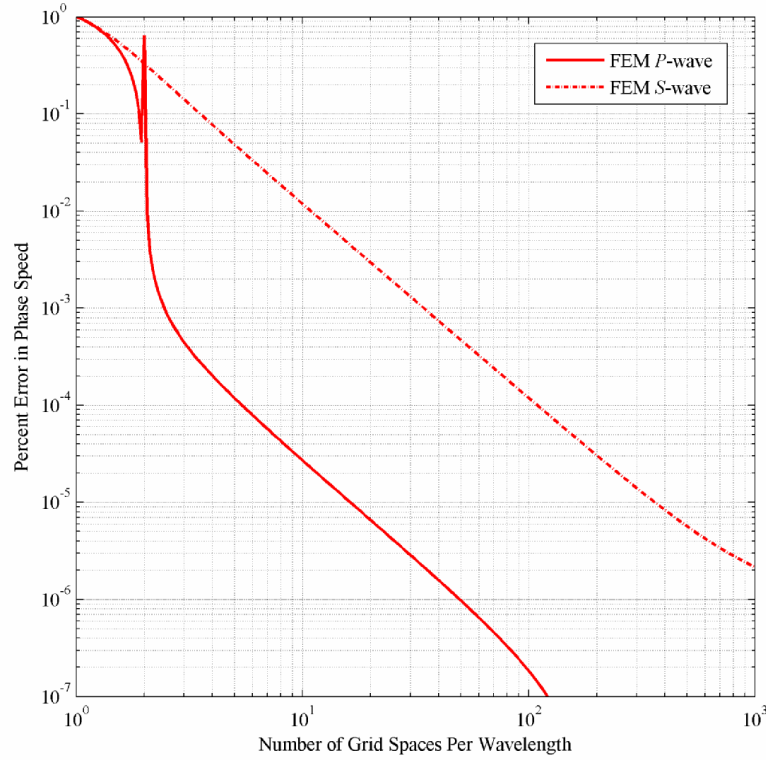
**Figure 17.** Percent error in phase speed as a function of grid spaces per wavelength, where $Q$=25, angle of orientation $\theta$ =45°.

## Computational cost of FEM and MSDLM models

Accuracy is not the only issue of importance for numerical simulation. Computational cost is another issue considered in this study. Theoretically, given enough time and computing power, extremely accurate numerical models can be generated using any numerical simulation method. In most engineering analyses, there are limits on time or computing power available for a specific model. A trade-off study can be completed in order to maximize accuracy while minimizing cost. In most cases, there comes a point where additional improvement in accuracy is not beneficial enough to justify the additional computational effort. This point varies depending on the type of engineering problem being analyzed.

One method of measuring computational cost is by estimating the number of floating point operations (FLOPS) per time step or iteration. For the FEM, the MSLM and the MSDLM, this involves determining the number of nodes and multiplying that number by the numerical operations (multiplies, adds, divides and subtracts) per node.

Since the FEM and MSLM use the Central Difference Method, the number of FLOPS can be easily determined. For the FEM, the number of numerical operations can be found by examining eqn. (6) and eqn. (7). The number of nodes can be determined by using the desired accuracy to find the number of elements needed to reach this accuracy. There are 38 numerical operations per time step per node for the FEM.

The discretized equations of motion for the MSLM are

$$
\rho \frac{{}^{t+\Delta t}u_{i,j} - 2\,{}^{t}u_{i,j} + {}^{t-\Delta t}u_{i,j}}{(\Delta t)^2} = \frac{\lambda+\mu}{h^2}\left({}^{t}u_{i+1,j} - 2\,{}^{t}u_{i,j} + {}^{t}u_{i-1,j}\right)
$$
$$
+ \frac{\mu}{2h^2}\left({}^{t}u_{i+1,j+1} + {}^{t}u_{i-1,j-1} + {}^{t}u_{i+1,j-1} + {}^{t}u_{i-1,j+1} - 4\,{}^{t}u_{i,j}\right) \qquad (37)
$$
$$
+ \frac{\lambda+\mu}{4h^2}\left({}^{t}v_{i+1,j+1} + {}^{t}v_{i-1,j-1} - {}^{t}v_{i+1,j-1} - {}^{t}v_{i-1,j+1}\right)
$$

$$
\rho \frac{{}^{t+\Delta t}v_{i,j} - 2\,{}^{t}v_{i,j} + {}^{t-\Delta t}v_{i,j}}{(\Delta t)^2} = \frac{\lambda+\mu}{h^2}\left({}^{t}v_{i,j+1} - 2\,{}^{t}v_{i,j} + {}^{t}v_{i,j-1}\right)
$$
$$
+ \frac{\mu}{2h^2}\left({}^{t}v_{i+1,j+1} + {}^{t}v_{i-1,j-1} + {}^{t}v_{i+1,j-1} + {}^{t}v_{i-1,j+1} - 4\,{}^{t}v_{i,j}\right) \qquad (38)
$$
$$
+ \frac{\lambda+\mu}{4h^2}\left({}^{t}u_{i+1,j+1} + {}^{t}u_{i-1,j-1} - {}^{t}u_{i+1,j-1} - {}^{t}u_{i-1,j+1}\right)
$$

There are 34 numerical operations per time step per node for the MSLM. Figure 18 is a plot of the number of FLOPS per $S$-Wavelength required for 1% phase speed error for S-waves as $v$ varies from 0.0 to 0.5 angle of incidence $\theta = 45°$.
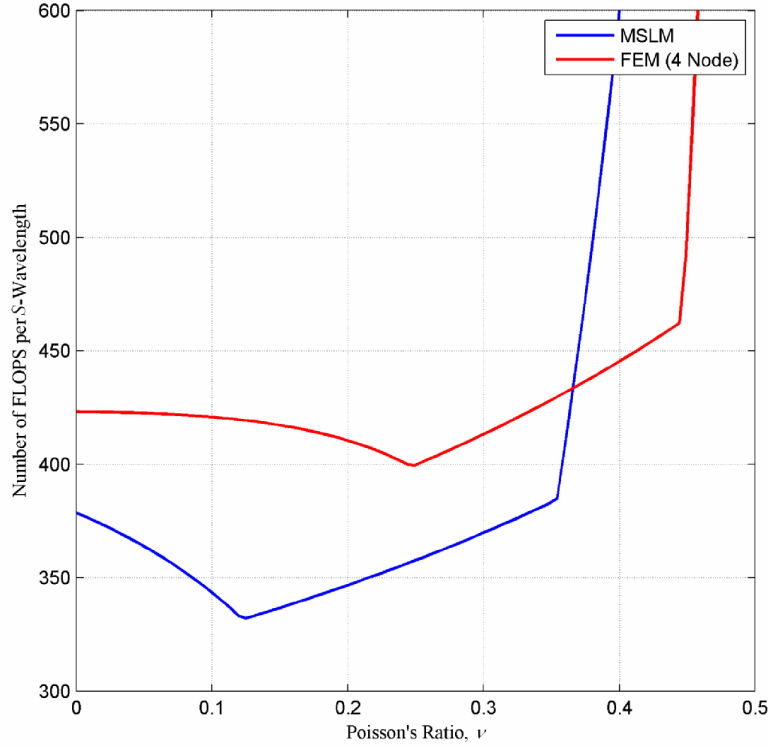
**Figure 18**. Number of FLOPS per *S*-Wavelength required for 1% phase speed error for S-waves as *v* varies from 0.0 to 0.5 angle of incidence $\theta = 45°$.

Determining the FLOPS for the MSDLM is more difficult, since the integration method used is a fourth order Runge-Kutta. Once the number of numerical operations is determined by examining eqn. (36) and eqn. (37), that number must be multiplied by four. Some computational savings are found since the MSDLM requires a Courant number of 1.3. This larger Courant number leads to a larger time step, therefore, there are fewer nodes in the model. The stress-dynamic equations for the MSDLM are

$$\frac{df_{i,j}^{x}}{dt} = -\frac{f_{i,j}^{x}}{\tau} + \frac{r(\Pi - M)}{\tau h^{2}}\left(u_{i+1,j} - 2u_{i,j} + u_{i-1,j}\right)$$

$$+ \frac{rM}{2\tau h^{2}}\left(u_{i+1,j+1} + u_{i-1,j-1} + u_{i+1,j-1} + u_{i-1,j+1} - 4u_{i,j}\right)$$

$$+ \frac{r(\Pi - M)}{4\tau h^{2}}\left(w_{i+1,j+1} + w_{i-1,j-1} - w_{i+1,j-1} - w_{i-1,j+1}\right)$$

$$+ \frac{\Pi - M}{h^{2}}\left(\dot{u}_{i+1,j} - 2\dot{u}_{i,j} + \dot{u}_{i-1,j}\right) \tag{39}$$

$$+ \frac{M}{2h^{2}}\left(\dot{u}_{i+1,j+1} + \dot{u}_{i-1,j-1} + \dot{u}_{i+1,j-1} + \dot{u}_{i-1,j+1} - 4\dot{u}_{i,j}\right)$$

$$+ \frac{\Pi - M}{4h^{2}}\left(\dot{w}_{i+1,j+1} + \dot{w}_{i-1,j-1} - \dot{w}_{i+1,j-1} - \dot{w}_{i-1,j+1}\right)$$

$$\frac{df_{i,j}^{z}}{dt} = -\frac{f_{i,j}^{z}}{\tau} + \frac{r(\Pi - M)}{\tau h^{2}}\left(w_{i,j+1} - 2w_{i,j} - w_{i,j-1}\right)$$

$$+ \frac{rM}{2\tau h^{2}}\left(w_{i+1,j+1} + w_{i-1,j-1} + w_{i+1,j-1} + w_{i-1,j-1} - 4w_{i,j}\right)$$

$$+ \frac{r(\Pi - M)}{4\tau h^{2}}\left(u_{i+1,j+1} + u_{i-1,j-1} - u_{i+1,j-1} - u_{i-1,j+1}\right)$$

$$+ \frac{\Pi - M}{h^{2}}\left(\dot{w}_{i,j+1} - 2\dot{w}_{i,j} - \dot{w}_{i,j-1}\right) \tag{40}$$

$$+ \frac{M}{2h^{2}}\left(\dot{w}_{i+1,j+1} + \dot{w}_{i-1,j-1} + \dot{w}_{i+1,j-1} + \dot{w}_{i-1,j-1} - 4\dot{w}_{i,j}\right)$$

$$+ \frac{\Pi - M}{4h^{2}}\left(\dot{u}_{i+1,j+1} + \dot{u}_{i-1,j-1} - \dot{u}_{i+1,j-1} - \dot{u}_{i-1,j+1}\right)$$

$$\frac{du_{i,j}}{dt} = \dot{u}_{i,j} \tag{41}$$

$$\frac{dw_{i,j}}{dt} = \dot{w}_{i,j} \tag{42}$$

$$\frac{d\dot{u}_{i,j}}{dt} = \frac{1}{\rho}\left(f_{i,j}^{bx} + f_{i,j}^{x}\right) \tag{43}$$

$$\frac{d\dot{w}_{i,j}}{dt} = \frac{1}{\rho}\left(f_{i,j}^{bz} + f_{i,j}^{z}\right) \tag{44}$$

There are 288 numerical operations per time step per node for the MSDLM. Stress-dynamic equations are used for the MSDLM to account for changes in volumetric forces. These forces must be included for the stress relaxation mechanism in the MSDLM.

The surface stress-dynamic equations for the MSDLM and the equations of motion for the FEM and the MSLM are different from the interior equations. For most engineering problems, the number of surface particles is minuscule compared to the number of interior particles and so are neglected in this study. The computational cost of a four-node FEM is approximately the same as that for the MSLM. The computational cost of the MSDLM is on the order of 5 times greater than the cost of the FEM and MSLM.

## Conclusions

Finite element, mass-spring lattice, and mass-spring-dashpot lattice models are powerful numerical simulation tools. For modeling elastic materials with Poisson's ratio between 0.0 and 0.2, the mass-spring lattice model has the lowest computational cost for phase speed error less than 1%. For modeling elastic materials with Poisson's ratio between 0.35 and 0.45, the finite element model is more accurate but costs just slightly more than the mass-spring lattice model. For modeling materials with attenuative properties, the MSDLM is more accurate but is nearly 5 times more expensive than the finite element model. Both the FEM and MSDLM model attenuative materials accurately.

# References

1.  Nguyen, L., J. Beach, and E. Greene. *International Maritime Defence Exhibition.* Singapore. (1999).

2.  Logan, C., *Advancing Technologies and Applications in Nondestructive Evaluation,* [Online] Available http://www.llnl.gov/str/Logan.html, (February 2, 2006).

3.  Hellier, C. *Handbook of Nondestructive Evaluation,* p. 7.110-7.111. McGraw-Hill Companies, Inc., New York (2001).

4.  Bathe, K, *Finite Element Procedures*, p. xiii. Prentice Hall, New Jersey, (1996).

5.  Yim, H and Y. Sohn, *Transactions on Ultrason. Ferroelectr. Freq. Cont*. 47:549 (2000).

6.  Small, P.D., *Ultrasonic Wave Propagation in Thick Layered Composites Containing Degraded Interfaces*, SM-NavE Thesis Massachusetts Institute of Technology, p.12 (2005).

7.  Yue, B and M. Guddati, *J. Acoust. Soc. Am.* 2132 (2005).

8.  Thomas, A., H. Yim and J.H. Williams, Jr. submitted for publication (2005).

9.  Yim, H. and Y. Sohn. *IEEE Trans. Ultrason. Ferroelectr. Freq. Cont*. 47:551 (2000).

10. Yim, H. and Y. Choi. *Mater. Eval*. 58:889 (2000).

11. Abraowitz and I.A. Stegun (Eds.), *Handbook of Mathematical Functions with Formulas, Graphs and Mathematical Tables*, p896-897. Dover, New York (1982).

12. Bathe, K. Finite Element Procedures. p815 Prentice Hall, Inc. (1996).

13. H. Yim. Unpublished research (2003).

14. Glaser, S. G. Weiss, L. Johnson *J. Acoust. Soc. Am*., 104 (3) (1998).

15. H. Lamb. *Philosophical Transactions of the Royal Society Of London. Series A, Containing Papers of a Mathematical or Physical Character.* **203**:1(1904).

# APPENDIX A - Derivation of the indicial notation for the 4-node finite element model

The finite element method (FEM) is a widely used tool in engineering analysis [A.1]. The four-node element is one of the simplest, but it is still a powerful and useful tool in the solution of practical engineering problems. In this appendix, a plane strain isotropic medium having mass- proportional damping is discretized.

The equations of motion in the interior of a plane strain isotropic medium having mass-proportional damping is expressed in Cartesian coordinates as

$$\rho \frac{\partial^2 u}{\partial t^2} = (\lambda + 2\mu) \frac{\partial^2 u}{\partial x^2} + (\lambda + \mu) \frac{\partial^2 v}{\partial x \partial y} + \mu \frac{\partial^2 u}{\partial y^2} - \frac{\rho}{\tau} \frac{\partial u}{\partial t} \qquad (A.1)$$

$$\rho \frac{\partial^2 v}{\partial t^2} = (\lambda + 2\mu) \frac{\partial^2 v}{\partial y^2} + (\lambda + \mu) \frac{\partial^2 u}{\partial x \partial y} + \mu \frac{\partial^2 v}{\partial x^2} - \frac{\rho}{\tau} \frac{\partial v}{\partial t} \qquad (A.2)$$

where $\rho$ is density, $u$ and $v$ are horizontal and vertical displacements, respectively, $\lambda$ and $\mu$ are Lamé elastic constants and $\tau$ is a characteristic time.

The corresponding elemental equilibrium equation for a lumped mass element can be expressed in matrix form as

$$\mathbf{M}^{(el)} \frac{{}^{t+\Delta t}\mathbf{u}^{(el)} - 2 {}^{t}\mathbf{u}^{(el)} + {}^{t-\Delta t}\mathbf{u}^{(el)}}{(\Delta t)^2} + \frac{1}{\tau} \mathbf{M}^{(el)} \frac{{}^{t+\Delta t}\mathbf{u}^{(el)} - {}^{t-\Delta t}\mathbf{u}^{(el)}}{2\Delta t} + \mathbf{K}^{(el)}\,{}^{t}\mathbf{u}^{(el)} = \mathbf{F}^{(el)} \qquad (A.3)$$

where $\mathbf{M}^{(el)}$ is the elemental mass matrix.

$$\mathbf{M}^{(el)} = \frac{\rho h^2}{4} \begin{bmatrix} 1 & & & & & & & \\ & 1 & & & & & & \\ & & 1 & & & & & \\ & & & 1 & & & & \\ & & & & 1 & & & \\ & & & & & 1 & & \\ & & & & & & 1 & \\ & & & & & & & 1 \end{bmatrix} \qquad (A.4)$$

and $^t\mathbf{u}^{(el)}$ is the elemental displacement vector

$$
^t\mathbf{u}^{(el)} = \begin{bmatrix} ^t u_1 \\ ^t u_2 \\ ^t u_3 \\ ^t u_4 \\ ^t v_1 \\ ^t v_2 \\ ^t v_3 \\ ^t v_4 \end{bmatrix}
\tag{A.5}
$$

A schematic of a square four-node element having grid spacing h is shown in Figure A1.
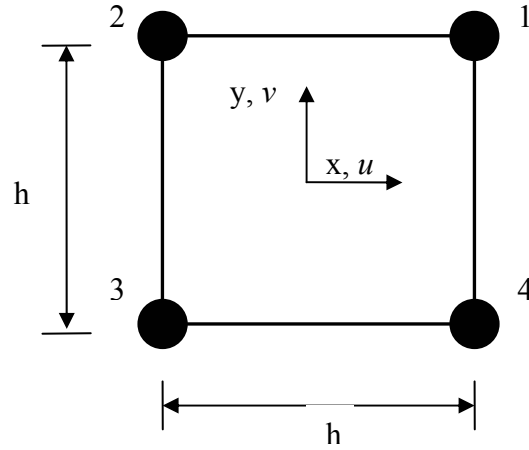


**Figure A 1.** Schematic of four-node element.

The elemental stiffness matrix $\mathbf{K}^{(el)}$ may be calculated as

$$
\mathbf{K}^{(el)} = \int_{-h/2}^{h/2} \int_{-h/2}^{h/2} \mathbf{B}^{(el)\mathbf{T}} \mathbf{C}^{(el)} \mathbf{B}^{(el)} dxdy
\tag{A.6}
$$

$\mathbf{H}^{(el)}$ is the displacement interpolation matrix for a four-node square element $i$ with sides of

length h

$$\mathbf{H}^{(el)} = \begin{bmatrix} h_1 & h_2 & h_3 & h_4 & 0 & 0 & 0 & 0 \\ 0 & 0 & 0 & 0 & h_1 & h_2 & h_3 & h_4 \end{bmatrix} \tag{A.7}$$

where

$$h_1 = \frac{1}{4}\left(1+\frac{2x}{h}\right)\left(1+\frac{2y}{h}\right) \tag{A.8}$$

$$h_2 = \frac{1}{4}\left(1-\frac{2x}{h}\right)\left(1+\frac{2y}{h}\right) \tag{A.9}$$

$$h_3 = \frac{1}{4}\left(1-\frac{2x}{h}\right)\left(1-\frac{2y}{h}\right) \tag{A.10}$$

$$h_4 = \frac{1}{4}\left(1+\frac{2x}{h}\right)\left(1-\frac{2y}{2h}\right) \tag{A.11}$$

$\mathbf{B}^{(el)}$ is the corresponding strain-displacement matrix corresponding to the local element degrees

of freedom, given as

$$\mathbf{B}^{(el)} = \begin{bmatrix} h_{1,x} & h_{2,x} & h_{3,x} & h_{4,x} & 0 & 0 & 0 & 0 \\ 0 & 0 & 0 & 0 & h_{1,y} & h_{2,y} & h_{3,y} & h_{4,y} \\ h_{1,y} & h_{2,y} & h_{3,y} & h_{4,y} & h_{1,x} & h_{2,x} & h_{3,x} & h_{4,x} \end{bmatrix} \tag{A.12}$$

where

45

$$h_{1,x} = \frac{1}{2} \frac{\left(1 + 2\frac{y}{h}\right)}{h} \tag{A.13}$$

$$h_{2,x} = \frac{-1}{2} \frac{\left(1 + 2\frac{y}{h}\right)}{h} \tag{A.14}$$

$$h_{3,x} = \frac{-1}{2} \frac{\left(1 - 2\frac{y}{h}\right)}{h} \tag{A.15}$$

$$h_{4,x} = \frac{1}{2} \frac{\left(1 - 2\frac{y}{h}\right)}{h} \tag{A.16}$$

$$h_{1,y} = \frac{1}{2} \frac{\left(1 + 2\frac{x}{h}\right)}{h} \tag{A.17}$$

$$h_{2,y} = \frac{1}{2} \frac{\left(1 - 2\frac{x}{h}\right)}{h} \tag{A.18}$$

$$h_{3,y} = \frac{-1}{2} \frac{\left(1 - 2\frac{x}{h}\right)}{h} \tag{A.19}$$

$$h_{4,y} = \frac{-1}{2} \frac{\left(1 + 2\frac{x}{h}\right)}{h} \tag{A.20}$$

$\mathbf{C}^{(el)}$ is the generalized stress-strain matrix for isotropic materials subject to plane strain

conditions, given as

$$\mathbf{C}^{(el)} = \begin{bmatrix} \lambda + 2\mu & \lambda & 0 \\ \lambda & \lambda + 2\mu & 0 \\ 0 & 0 & \mu \end{bmatrix} \tag{A.21}$$

The elemental **K** matrix is

$$
\mathbf{K}^{(el)} =
\begin{bmatrix}
k_1 & k_2 & k_3 & k_4 & k_5 & k_6 & k_7 & k_8 \\
 & k_1 & k_4 & k_3 & k_8 & k_7 & k_6 & k_5 \\
 & & k_1 & k_2 & k_7 & k_8 & k_5 & k_6 \\
 & & & k_1 & k_6 & k_5 & k_8 & k_7 \\
 & & & & k_1 & k_4 & k_3 & k_2 \\
 & & & & & k_1 & k_2 & k_3 \\
 & & & & & & k_1 & k_4 \\
 & & & & & & & k_1
\end{bmatrix}
\tag{A.22}
$$

where

$$
k_1 = \frac{1}{3}\lambda + \mu
\tag{A.23}
$$

$$
k_2 = \frac{-1}{3}\lambda - \frac{1}{2}\mu
\tag{A.24}
$$

$$
k_3 = \frac{-1}{6}\lambda - \frac{1}{2}\mu
\tag{A.25}
$$

$$
k_4 = \frac{1}{6}\lambda
\tag{A.26}
$$

$$
k_5 = \frac{1}{4}\lambda + \frac{1}{4}\mu
\tag{A.27}
$$

$$
k_6 = \frac{1}{4}\lambda - \frac{1}{4}\mu
\tag{A.28}
$$

$$
k_7 = -\frac{1}{4}\lambda - \frac{1}{4}\mu
\tag{A.29}
$$

$$k_8 = -\frac{1}{4}\lambda + \frac{1}{4}\mu$$

(A.30)

*Interior Element*

Through careful examination of the matrices centered at $(i,j)$, the global degrees of freedom can be identified through use of the local degrees of freedom and the matrices listed above.
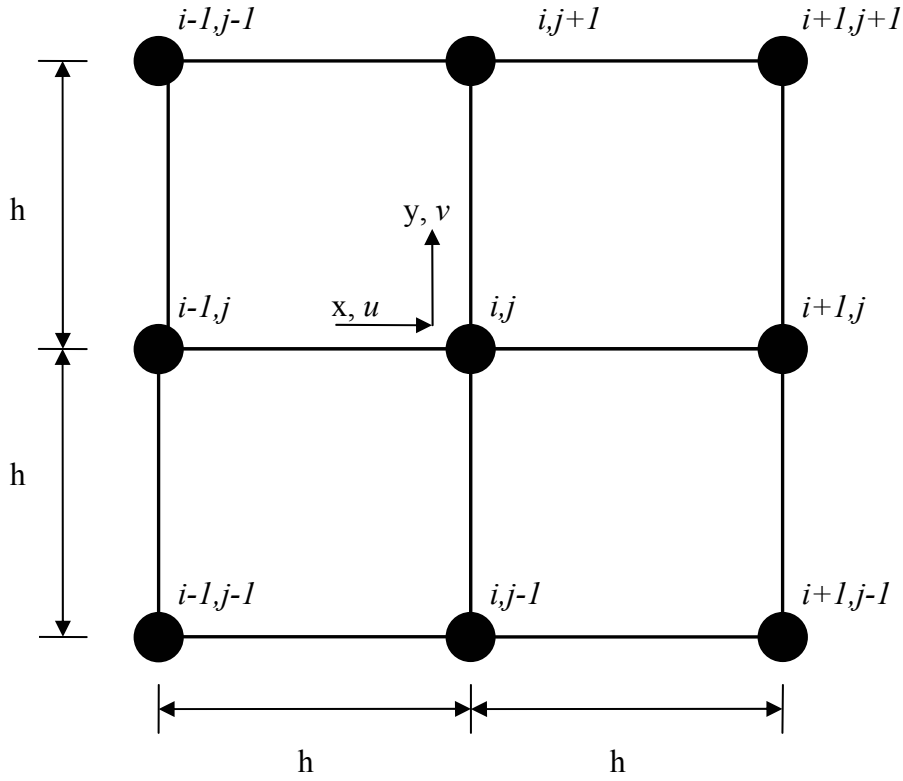


**Figure A 2.** Interior elemental matrices centered at position $(i,j)$.

The four-node finite element discretization of eqns. (A.1) and (A. 2) yields the following equations written in component form at position $(i,j)$ and time $t$.
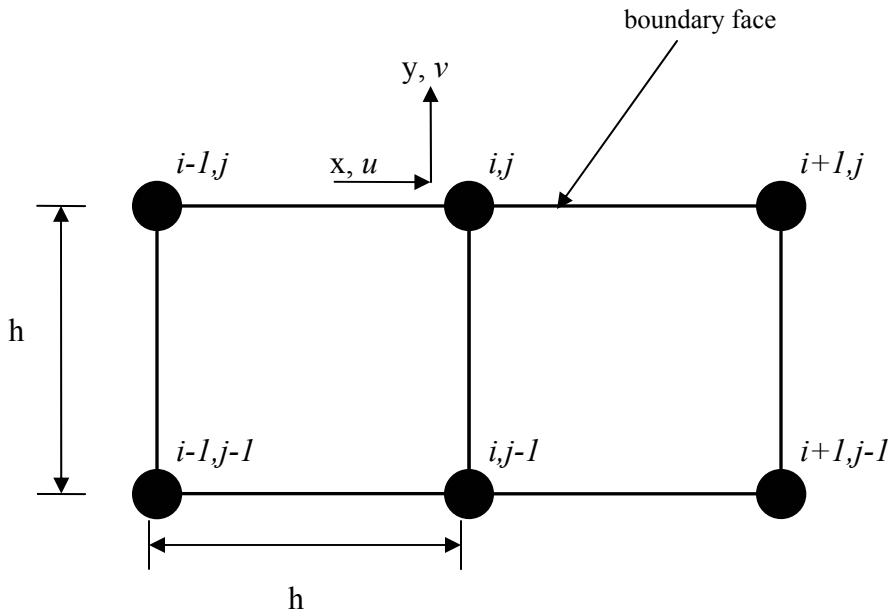
$$
\rho \frac{1}{\Delta t^2}\left( {}^{t-\Delta t}u_{i,j} - 2\,{}^{t}u_{i,j} + {}^{t+\Delta t}u_{i,j}\right) = \frac{\frac{2}{3}\lambda + \mu}{h^2}\left( {}^{t}u_{i+1,j} + {}^{t}u_{i-1,j} - 2\,{}^{t}u_{i,j}\right)
$$
$$
- \frac{\frac{1}{3}\lambda}{h^2}\left( {}^{t}u_{i,j+1} + {}^{t}u_{i,j-1} - 2\,{}^{t}u_{i,j}\right)
$$
$$
+ \frac{\frac{1}{6}\lambda + \frac{1}{2}\mu}{h^2}\left( {}^{t}u_{i+1,j+1} + {}^{t}u_{i-1,j+1} + {}^{t}u_{i-1,j-1} + {}^{t}u_{i+1,j-1} - 4\,{}^{t}u_{i,j}\right) \qquad \text{(A.31)}
$$
$$
+ \frac{\frac{1}{4}\lambda + \frac{1}{4}\mu}{h^2}\left( {}^{t}v_{i+1,j+1} - {}^{t}v_{i-1,j+1} + {}^{t}v_{i-1,j-1} - {}^{t}v_{i+1,j-1}\right)
$$
$$
- \frac{\rho}{\tau}\frac{1}{2\Delta t}\left( -{}^{t-\Delta t}u_{i,j} + {}^{t+\Delta t}u_{i,j}\right)
$$

$$
\rho \frac{1}{\Delta t^2}\left( {}^{t-\Delta t}v_{i,j} - 2\,{}^{t}v_{i,j} + {}^{t+\Delta y}v_{i,j}\right) = \frac{\frac{2}{3}\lambda + \mu}{h^2}\left( {}^{t}v_{i,j+1} + {}^{t}v_{i,j-1} - {}^{t}2v_{i,j}\right)
$$
$$
- \frac{\frac{1}{3}\lambda}{h^2}\left( {}^{t}v_{i+1,j} + {}^{t}v_{i-1,j} - 2\,{}^{t}v_{i,j}\right)
$$
$$
+ \frac{\frac{1}{6}\lambda + \frac{1}{2}\mu}{h^2}\left( {}^{t}v_{i+1,j+1} + {}^{t}v_{i+1,j-1} + {}^{t}v_{i-1,j-1} + {}^{t}v_{i-1,j+1} - 4\,{}^{t}v_{i,j}\right) \qquad \text{(A.32)}
$$
$$
+ \frac{\frac{1}{4}\lambda + \frac{1}{4}\mu}{h^2}\left( {}^{t}u_{i+1,j+1} - {}^{t}u_{i+1,j-1} + {}^{t}u_{i-1,j-1} - {}^{t}u_{i-1,j+1}\right)
$$
$$
- \frac{\rho}{\tau}\frac{1}{2\Delta t}\left( -{}^{t-\Delta t}v_{i,j} + {}^{t+\Delta t}v_{i,j}\right)
$$

where $\Delta t$ is the numerical time step.

*Surface Element*

Through examination of the matrices centered at (*i,j*), the global degrees of freedom can be identified through use of the local degrees of freedom. A two-dimensional schematic of the FEM discretization of a plane strain elastic solid along a traction boundary is shown in Figure A 3.

**Figure A 3.** Schematic of a surface element centered at (i,j).

The corresponding equations of motion are

$$\rho\frac{1}{\Delta t^{2}}\left({}^{t-\Delta t}u_{i,j}-2{}^{t}u_{i,j}+{}^{t+\Delta t}u_{i,j}\right)+\frac{\rho}{\tau}\frac{1}{2\Delta t}\left(-{}^{t-\Delta t}u_{i,j}+{}^{t+\Delta t}u_{i,j}\right)=\frac{\frac{2}{3}\lambda+\mu}{h^{2}}\left({}^{t}u_{i+1,j}+{}^{t}u_{i-1,j}-2{}^{t}u_{i,j}\right)$$

$$-\frac{\frac{2}{3}\lambda}{h^{2}}\left({}^{t}u_{i,j-1}-{}^{t}u_{i,j}\right)$$

$$+\frac{\frac{1}{3}\lambda+\mu}{h^{2}}\left({}^{t}u_{i-1,j-1}+{}^{t}u_{i+1,j-1}-2{}^{t}u_{i,j}\right) \tag{A.33}$$

$$+\frac{\frac{1}{2}\lambda+\frac{1}{2}\mu}{h^{2}}\left({}^{t}v_{i-1,j-1}-{}^{t}v_{i+1,j-1}\right)-\frac{\frac{1}{2}\lambda-\frac{1}{2}\mu}{h^{2}}\left({}^{t}v_{i-1,j}-{}^{t}v_{i+1j}\right)$$


$$\rho\frac{1}{\Delta t^{2}}\left({}^{t-\Delta t}v_{i,j}-2{}^{t}v_{i,j}+{}^{t+\Delta y}v_{i,j}\right)+\frac{\rho}{\tau}\frac{1}{2\Delta t}\left(-{}^{t-\Delta t}v_{i,j}+{}^{t+\Delta t}v_{i,j}\right)=\frac{\frac{4}{3}\lambda+2\mu}{h^{2}}\left({}^{t}v_{i,j-1}-{}^{t}v_{i,j}\right)$$

$$-\frac{\frac{1}{3}\lambda}{h^{2}}\left({}^{t}v_{i-1,j}+{}^{t}v_{i+1,j}-2{}^{t}v_{i,j}\right)$$

$$+\frac{\frac{1}{3}\lambda+\mu}{h^{2}}\left({}^{t}v_{i-1,j-1}+{}^{t}v_{i+1,j-1}-2{}^{t}v_{i,j}\right) \tag{A.34}$$

$$+\frac{\frac{1}{2}\lambda+\frac{1}{2}\mu}{h^{2}}\left({}^{t}u_{i-1,j-1}-{}^{t}u_{i+1,j-1}\right)-\frac{\frac{1}{2}\lambda-\frac{1}{2}\mu}{h^{2}}\left({}^{t}u_{i+1,j}-{}^{t}u_{i-1,j}\right)$$

Where $\Delta t$ is the numerical time step, and $u_{i,j}$ and $v_{i,j}$ are the horizontal and vertical displacements, respectively.


REFERENCES


[A-1]   Bathe, K, *Finite Element Procedures*, Prentice Hall, New Jersey, 1996.

Page intentionally left blank

# APPENDIX B - Dispersion Relation/ High frequency assumption

In order to make numerical analysis of elastic wave phenomena possible, assumptions concerning the dispersion relation and frequency of the wave must be made. In this appendix, the dispersion relation for a material having mass-proportional damping is derived.

*Equilibrium equation*

The equation of motion for a one-dimensional material having mass-proportional damping is

$$E\,\partial^2 u / \partial x^2 + \frac{\rho}{\tau} \partial u / \partial x = \rho\,\partial^2 u / \partial t^2 \tag{B.1}$$

where $E$ is the governing elastic constant, $u$ is the displacement, $\rho$ is the density, and $\tau$ is a characteristic time.

Consider a propagating harmonic wave having the form

$$u(x,t) = U_o e^{-\alpha x + i(kx - \omega t)} \tag{B.2}$$

where $U_o$ is the peak displacement, $\alpha$ is the attenuation, $k$ is the wavenumber, and $\omega$ is the radial frequency.

Solving for the partial derivatives yields

$$\partial^2 u / \partial x^2 = U_o(\alpha^2 - k^2)e^{-\alpha x + i(kx - \omega t)} - U_o(2\alpha i k)e^{-\alpha x + i(kx - \omega t)} \tag{B.3}$$

$$\partial u / \partial t = U_o i\omega e^{-\alpha x + i(kx - \omega t)} \tag{B.4}$$

$$\partial^2 u / \partial t^2 = -U_o \omega^2 e^{-\alpha x + i(kx - \omega t)} \tag{B.5}$$

After substituting eqns. (B.3) through (B.5) into eqn. (B.1) and simplifying, the dispersion relation becomes

$$E(\alpha^2 - k^2) + \rho\omega^2 = E(2\alpha ik) - \frac{\rho}{\tau}i\omega \tag{B.6}$$

Separating the real and imaginary parts of eqn. (B.6) yields

$$E(\alpha^2 - k^2) + \rho\omega^2 = 0 \tag{B.7}$$

$$E(2\alpha ik) - \frac{\rho}{\tau}i\omega = 0 \tag{B.8}$$

Solving eqn. (B.8) for the wavenumber yields

$$k = \frac{\rho\omega}{\tau E 2\alpha} \tag{B.9}$$

Substituting eqn. (B.9) into eqn. (B.7) yields

$$\frac{E\left(\alpha^2 - \left(\frac{\rho\omega}{\tau E 2\alpha}\right)^2\right)}{\rho} + \omega^2 = 0 \tag{B.10}$$

Let

$$\frac{E}{\rho} = c^2_{max} \tag{B.11}$$

Multipyling eqn (B.10) by $\alpha^2$ and substituting eqn. (B.11) into eqn. (B.10) yields

$$\alpha^4 - \frac{\omega^2}{\tau^2 4 c_{max}^4} + \frac{\omega^2\alpha^2}{c_{max}^2} = 0 \tag{B.12}$$

Solving for $\alpha^2$ yields

$$\alpha^2 = \frac{\omega^2}{2c_{max}^2}\left(-1 + \sqrt{1 + \frac{1}{\tau^2\omega^2}}\right) \qquad \text{(B.13)}$$

Substituting eqn (B.13) into eqn. (B.7) yields

$$k^2 = \frac{\omega^2}{2c_{max}^2}\left(1 + \sqrt{1 + \frac{1}{\tau^2\omega^2}}\right) \qquad \text{(B.14)}$$

At high frequencies,

$$k \rightarrow \frac{\omega}{c_{max}} \qquad \text{(B.15)}$$

$$\alpha \rightarrow \frac{1}{2c_{max}\tau} \qquad \text{(B.16)}$$

At low frequencies,

$$k \rightarrow \frac{1}{2\tau c_{max}} \qquad \text{(B.17)}$$

$$\alpha \rightarrow \sqrt{\frac{\omega}{2c_{max}^2\tau}}$$

Page intentionally left blank

# APPENDIX C - Lamb's Solution

This appendix summarizes Lamb's solution for surface displacements due to surface excitation [C-1]. Consider a normal point line source, having peak magnitude $Q$ and temporal variation $q(t)$, acting at the origin of a half-space ($y<0$) having Lamé constants $\lambda$ and $\mu$, and density $\rho$.

For $x \leq 0$, the horizontal and vertical surface displacements, $u$ and $v$ respectively, are

$$u = -\frac{Q}{\mu}Hq(t - s_R x) - \frac{Q}{\mu}\frac{2}{\pi}\int_{s_L}^{s_T}\frac{s_T^2\theta(2\theta^2 - s_T^2)\sqrt{\theta^2 - s_L^2}\sqrt{s_T^2 - \theta^2}}{(2\theta^2 - s_T^2)^4 + 16\theta^4(\theta^2 - s_L^2)(s_T^2 - \theta^2)}q(t - \theta x)d\theta \qquad (C.1)$$

$$v = \frac{Q}{\mu}\frac{1}{\pi}\int_{s_L}^{s_T}\frac{s_T^2(2\theta^2 - s_T^2)\sqrt{\theta^2 - s_L^2}}{(2\theta^2 - s_T^2)^4 + 16\theta^4(\theta^2 - s_L^2)(s_T^2 - \theta^2)}q(t - \theta x)d\theta$$

$$+ \frac{Q}{\mu}\frac{1}{\pi}P\int_{s_T}^{\infty}\frac{s_T^2\sqrt{\theta^2 - s_L^2}}{(2\theta^2 - s_T^2)^2 - 4\theta^2\sqrt{\theta^2 - s_L^2}\sqrt{\theta^2 - s_T^2}}q(t - \theta x)d\theta \qquad (C.2)$$

where $s_T$ is the transverse wave slowness (inverse wave velocity) given by

$$s_T = \sqrt{\frac{\rho}{\mu}} \qquad (C.3)$$

$s_L$ is the longitudinal wave slowness given by

$$s_L = \sqrt{\frac{\rho}{\lambda + 2\mu}} \qquad (C.4)$$

$s_R$ is the Rayleigh wave slowness given by the real root of the equation

$$(2s_R^2 - s_T^2)^2 - 4s_R^2\sqrt{s_R^2 - s_L^2}\sqrt{s_R^2 - s_T^2} = 0 \qquad (C.5)$$

Also,

$$H = -\frac{s_R\left(2s_R^2 - s_T^2 - 2\sqrt{s_R^2 - s_L^2}\sqrt{s_R^2 - s_T^2}\right)}{F} \qquad (C.6)$$

where

$$F = \frac{4\left(-2s_L{}^2 s_T{}^2 s_R + 3\left(s_L{}^2 + s_T{}^2\right)s_R{}^3 - 4s_R{}^5 + 4s_R{}^3\sqrt{s_R{}^2 - s_L{}^2}\sqrt{s_R{}^2 - s_T{}^2}\right)}{\sqrt{s_R{}^2 - s_L{}^2}\sqrt{s_R{}^2 - s_T{}^2}} - 8s_T{}^2 s_R \quad \text{(C.7)}$$

$P$ in eqn. (C.2) denotes the principal value of the integral [C-2]. A non-integrable singularity

exists at $\theta = s_R$ and the integral must be defined as

$$P\int_a^b f(\xi)d\xi = \lim_{\varepsilon \to 0}\left(\int_a^{c-\varepsilon} f(\xi)d\xi + \int_{c+\varepsilon}^b f(\xi)d\xi\right) \quad \text{(C.8)}$$

where $a<c<b$ and the non-integrable singularity exists at $f(c)$.

The surface displacements for x<0 are given by replacing $\left(t - \zeta x\right)$ with $\left(t + \zeta x\right)$ in eqns.

(C.1) and (C.2) and reversing the sign of the horizontal displacements in eqn. (C.1).


REFERENCES

[C-1]   H. Lamb. *Philosophical Transactions of the Royal Society of London. Series A, Containing Papers of a Mathematical or Physical Character*. **203**:1 (1904).

[C-2]   E. Kreyszig. Advanced Engineering Mathematics 7th ed., p.851. John Wiley& Sons, New York (1993).

# APPENDIX D - Penetration Depth

Let the penetration depth $Q$ of an attenuative material be the number of wavelengths required for a cyclic input signal to decrease in amplitude to $e^{-\pi}$ where $\alpha$ is the attenuation and $x$ is the distance.

$$e^{-\alpha Q \lambda} = e^{-\pi} \tag{D.1}$$

where $\lambda$ is the wavelength

$$\alpha Q \lambda = \pi \tag{D.2}$$

$$Q = \frac{\pi}{\alpha \lambda} \tag{D.3}$$

For a standard linear solid [D1] having a relaxation time $\tau$, under the frequency assumption

$$\omega \tau >> 1 \tag{D.4}$$

where $\omega$ is the circular frequency. Frequency-independent attenuation is

$$\alpha = \frac{1}{2\tau c} \tag{D.5}$$

where $c$ is maximum phase speed. Recall,

$$c = \lambda f \tag{D.6}$$

where $f$ is cyclic frequency. The relationship between $\omega$ and $f$ is

$$\omega = 2\pi f \tag{D.7}$$

therefore

$$f = \frac{\omega}{2\pi} \tag{D.8}$$

Substituting eqn. (D-5) into eqn. (D-3) yields

$$\frac{\pi 2\tau c}{\lambda} = Q \tag{D.9}$$

Substituting eqn. (D-6) into eqn. (D-9) yields

$$\pi 2\tau f = Q \tag{D.10}$$

Substituting eqn. (D-8) into (D-10) yields

$$\tau \omega = Q \tag{D.11}$$

Recall,

$$c = \frac{\omega}{k} \tag{D.12}$$

where $k$ is the wavenumber. $k$ can be rewritten as

$$k = \frac{\omega}{\sqrt{2}c_{max}} \left( 1 + \sqrt{1 + \frac{1}{\omega^2 \tau^2}} \right)^{\frac{1}{2}} \tag{D.13}$$

The phase speed error between the exact solution and the numerical approximation can be
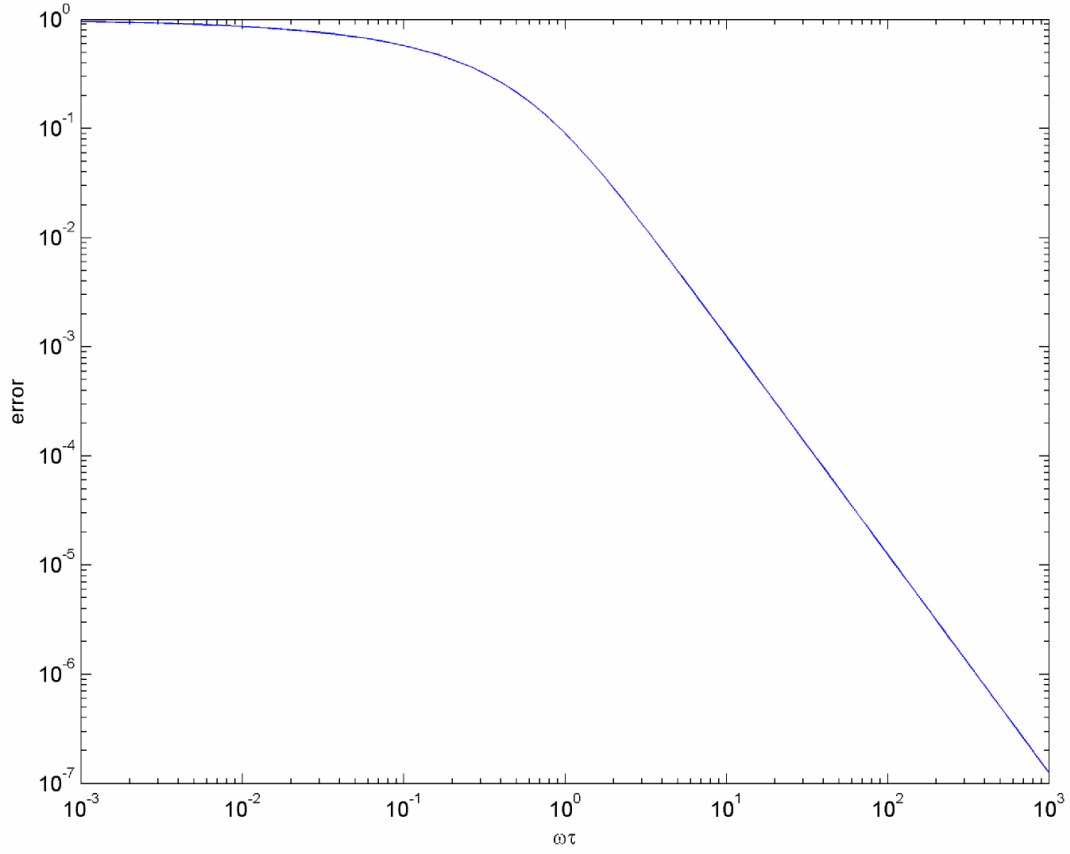
written as

$$error = \frac{c - c_{max}}{c_{max}} \tag{D.14}$$

Substituting eqn. (D-12) into (D-14) yields

$$error = \frac{\frac{\omega}{k} - c_{max}}{c_{max}} \tag{D.15}$$

Substituting eqn. (D-13) into (D-15) yields

$$error = \sqrt{2} \left( 1 + \sqrt{1 + \frac{1}{\omega^2 \tau^2}} \right)^{-\frac{1}{2}} - 1 \tag{D.16}$$

Figure D 1 is a plot of the error with respect to $\omega \tau$. The error decreases as the frequency

increases. As $\omega \tau$ increases, Q increases. Therefore a material having a high penetration depth,

which is equivalent to a low attenuation, is modeled more accurately.

**Figure D 1.** Phase speed error as a function of $\omega\tau$.

*Error in attenuation*

Attenuation may be written as

$$\alpha = \frac{\omega}{\sqrt{2}c_{max}}\left(-1+\sqrt{1+\frac{1}{\omega^2\tau^2}}\right)^{1/2} \tag{D.17}$$

recall that numerically

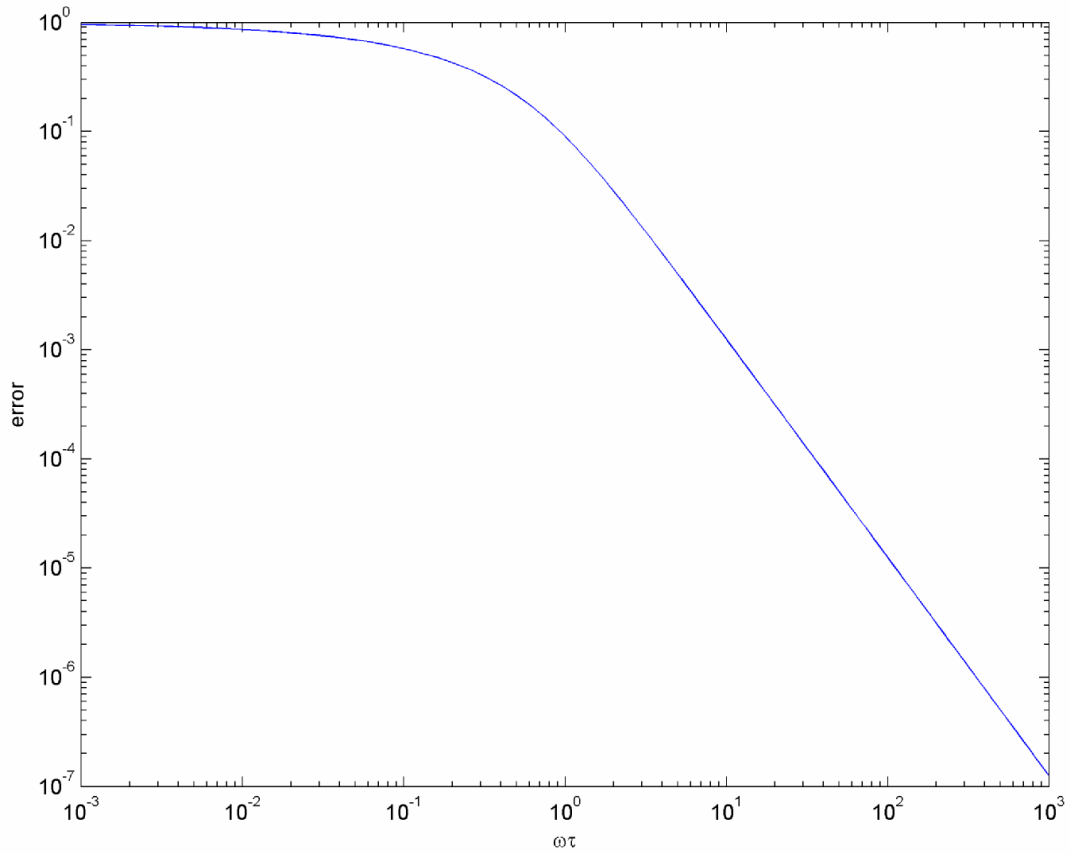$$\alpha_{max} = \frac{1}{2\tau c_{max}} \tag{D.18}$$

The error between the exact and numerical attenuation can be written as

$$error = \frac{\alpha_{\max} - \alpha}{\alpha_{\max}} \qquad (D.19)$$

Substituting eqn. D-18 and C-19 into eqn. D-17 yields

$$error = 1 - \sqrt{2}\tau\left(-1 + \sqrt{1 + \frac{1}{\omega^2\tau^2}}\right)^{\frac{1}{2}} \qquad (D.20)$$

Figure D 2 is a plot of the attenuation error as a function of $\omega\tau$. As $\omega\tau$ increases, the error decreases.



**Figure D 2.** Attenuation error as a function of $\omega\tau$.

If a material is attenuative, its penetration depth decreases. Since penetration depth is a function of $\omega\tau$, the frequency decreases as well. This decrease in frequency causes errors in phase speed modeling.

REFERENCES

[D-1]  Thomas, A., H. Yim and J.H. Williams, Jr. submitted for publication (2005).

Page intentionally left blank